J. Math. Biol. 42, 387–423 (2001)
Digital Object Identifier (DOI):
10.1007/s002850000067

Mathematical Biology

M.A.J. Chaplain · M. Ganesh · I.G. Graham

Spatio-temporal pattern formation on spherical surfaces: numerical simulation and application to solid tumour growth

Received: 27 July 2000 / Revised version: 15 August 2000 /
Published online: 16 February 2001 –

Abstract. In this paper we examine spatio-temporal pattern formation in reaction-diffusion systems on the surface of the unit sphere in 3D. We first generalise the usual linear stability analysis for a two-chemical system to this geometrical context. Noting the limitations of this approach (in terms of rigorous prediction of spatially heterogeneous steady-states) leads us to develop, as an alternative, a novel numerical method which can be applied to systems of any dimension with any reaction kinetics. This numerical method is based on the method of lines with spherical harmonics and uses fast Fourier transforms to expedite the computation of the reaction kinetics. Numerical experiments show that this method efficiently computes the evolution of spatial patterns and yields numerical results which coincide with those predicted by linear stability analysis when the latter is known. Using these tools, we then investigate the rôle that pre-pattern (Turing) theory may play in the growth and development of solid tumours. The theoretical steady-state distributions of two chemicals (one a growth activating factor, the other a growth inhibitory factor) are compared with the experimentally and clinically observed spatial heterogeneity of cancer cells in small, solid spherical tumours such as multicell spheroids and carcinomas. Moreover, we suggest a number of chemicals which are known to be produced by tumour cells (autocrine growth factors), and are also known to interact with one another, as possible growth promoting and growth inhibiting factors respectively. In order to connect more concretely the numerical method to this application, we compute spatially heterogeneous patterns on the surface of a growing spherical tumour, modelled as a moving-boundary problem. The numerical results strongly support the theoretical expectations in this case. Finally in an appendix we give a brief analysis of the numerical method.

1. Introduction

Since Turing's seminal paper in 1952 [74], reaction-diffusion (RD) pre-pattern theory has been proposed as a mechanism to describe spatio-temporal pattern formation in many biological systems. Specific applications of the theory (to name

M.A.J. Chaplain: Department of Mathematics, University of Dundee, Dundee DD1 4HN, UK. e-mail: chaplain@maths.dundee.ac.uk

M. Ganesh: School of Mathematics, University of New South Wales, Sydney, NSW 2052, Australia. e-mail: ganesh@maths.unsw.edu.au

I.G. Graham: Department of Mathematical Sciences, University of Bath, Bath BA2 7AY, UK. e-mail: igg@maths.bath.ac.uk

Key words: Pattern formation – Solid tumour growth

but a few) can be found in processes in developmental biology, population biology, ecology and interacting chemical systems. It is not our intention here to discuss these applications – for a comprehensive account of the theory and references to many other applications, the interested reader is referred to the books [6], [40], [41], [49]. However, in spite of its apparent success in explaining the appearance of spatial heterogeneity in many biological systems, there are still some serious drawbacks with the theory. For example, there is the so-called problem of robustness – the solution patterns obtained from RD systems (with zero flux boundary conditions) are known to be sensitive to changes in the initial conditions and the size and shape of the domain – and in many cases there is also the problem of actually identifying specific chemicals. Moreover, much of the analysis of reaction-diffusion theory in the mathematical biology literature has been carried out on simple domains in one and two-space dimensions.

The aims of this paper are as follows:

(i) to develop an appropriate general numerical method for examining reaction-diffusion equations on the surface of a sphere.
(ii) to apply the reaction-diffusion pre-pattern theory to a suitable problem on a spherical domain, that of an avascular solid tumour; to suggest actual chemicals known to be produced by tumours (autocrine growth factors) which could give rise to the pre-patterns; to compare the predicted pre-pattern results with those computed numerically and examine their relevance in the light of clinical and experimental observations.
(iii) to model the problem of a growing solid tumour (using a moving boundary formulation of the problem); to analyse numerically the system of reaction-diffusion equations on a growing, spherical domain; to discuss the implications of the results in terms of the observed patterns of invasion and metastasis of cancers.

Since much of the analysis in the current theoretical biology literature concerning the application of reaction-diffusion systems (pre-pattern theory) to biological problems is based on linear stability theory, it does not give a rigorous mathematical prediction of the spatially heterogeneous steady-state patterns in RD systems (cf. [49]). Moreover, by its nature, this analysis has to be developed separately for each set of reaction kinetics. Numerical simulations on the other hand may be applied to any kinetics. However, up until now they have mostly been applied to RD systems on simple Euclidean domains in 1D or 2D, such as an interval or a square, and 3D problems have been tackled only at the expense of considerable computing power [28–32]. The nature of the application which we have in mind here (solid tumour growth) dictates that the natural spatial domain can be taken to be a closed 2D manifold in 3D space. Thus in this paper we develop such a numerical method for the simplest such manifold – the surface of the unit sphere $S = \{\mathbf{x} \in \mathbb{R}^3 : |\mathbf{x}| = 1\}$. While this choice is convenient for our method, it is still of great relevance for applications. Our method can in principle also be extended to more general surfaces although this would involve additional numerical work. As we shall see, our numerical method provides a fast solver for this class

of RD systems and presents a considerable improvement over existing technology for such problems (cf. [43]).

The generic reaction-diffusion system which we will analyse numerically in this paper is written:

$$\mathbf{u}_t = D\Delta_*\mathbf{u} + \mathbf{f}(\mathbf{u}) \tag{1.1}$$

on the space-time domain $(\mathbf{x}, t) \in S \times [0, \infty)$, where $(u_1, \ldots, u_s)^T = \mathbf{u} = \mathbf{u}(\mathbf{x}, t)$ is a vector (for example, of chemical concentrations such as growth factors), $D = \text{diag}\{d_1, \ldots, d_s\}$ is a diagonal matrix of positive diffusion coefficients, Δ_* is the Laplace-Beltrami operator:

$$\Delta_* u = \frac{1}{\sin\theta}\left\{\frac{\partial}{\partial\theta}\left(\sin\theta\frac{\partial u}{\partial\theta}\right) + \frac{1}{\sin\theta}\frac{\partial^2 u}{\partial\phi^2}\right\},$$

and $\mathbf{f} : \mathbb{R}^s \to \mathbb{R}^s$ is a (nonlinear) vector-valued function representing the reaction kinetics (cf. [49]). We assume that $\mathbf{f}$ is autonomous, that is,

$$\mathbf{f}(\mathbf{u})(\mathbf{x}, t) = \mathbf{f}(\mathbf{u}(\mathbf{x}, t)), \quad (\mathbf{x}, t) \in S \times [0, \infty).$$

The numerical experiments in this paper are restricted to the special two-species case

$$\begin{aligned} u_t &= \Delta_* u + \gamma f(u, v), \\ v_t &= d\Delta_* v + \gamma g(u, v), \end{aligned} \tag{1.2}$$

with d, γ given positive parameters and f, g given functions, but in fact the method applies equally well to any number of chemical species. In general system (1.1) arises naturally in studies of pre-pattern formation in biological systems. There it is of interest to study the stability of spatially homogeneous steady states of (1.1) with respect to the diffusion represented by $D\Delta_*\mathbf{u}$, and in particular to identify spatial patterns which evolve in practice from unstable (in the Turing sense, defined in the next section) homogeneous steady states.

Our numerical method for (1.1) consists of a classical method of lines approach, with the spatial dependence modelled using surface spherical harmonics. The resulting system of ordinary differential equations is solved by a stiff solver – in this case ODE15s from the MATLAB ODE Suite, which is based on *numerical differentiation formulae* of order 1 to 5 [62]. The exponential (in space) convergence of spherical harmonic approximation means that we have to solve only relatively small systems of ordinary differential equations (typically of order 100 in size) and simulations of the special case (1.2) took times of the order of minutes on an up-to-date platform. The method of lines, although simple and popular, can be expensive, especially if the numerical realisation of the reaction kinetics ($\mathbf{f}$ in (1.1)) is complicated. The chief novel feature here is the fast implementation of the kinetics using Fast Fourier Transforms (FFT), and this is the main ingredient leading to reasonable run times achieved by our code. We test our code by verifying that the numerical results for (1.2) coincide with the predictions of linear stability analysis, when this is known.

Having developed a suitable efficient numerical method for (1.1), we turn our attention to applying pre-pattern theory to the growth and development of solid

tumours. In this case, many of the problems associated with pattern formation in reaction-diffusion systems (for example, robustness of patterns, identification of chemicals) are absent and the modelling is an extension of the work of [12]. Concerning the appropriateness of the application of this theory to solid tumour growth, we note that; (i) there is a definite observed spatial heterogeneity of solid tumours in terms of regions of cell proliferation [5, 24, 35, 51, 61, 77]; (ii) there is a known involvement of specific chemicals, or cytokines, produced by the tumour cells themselves (autocrine growth factors) [69], which (a) have opposite effects on cancer cells in terms of proliferation (stimulatory or inhibitory) and (b) interact with each other [10, 13, 17, 21, 22, 26, 36], [55]–[57], [58], [59], [64, 66, 68, 78]; (iii) in the case of solid tumour growth there is an identifiable transition between two different growth phases (the avascular growth phase and the vascular growth phase) in which there is a clear domain (size)-dependence; (iv) in terms of scale, the growth of the avascular nodules occurs at a scale of up to a few millimetres in diameter, giving a scale of tenths of millimetres for the width of a "patch" of peak concentration of chemical (cf. actual *in vitro* experiments of [16]); (v) there is a certain relationship/correspondence between cellular events in developmental processes (where there have been many previous applications of pre-pattern theory) and cancer (in some sense, cancer is development which is out of control).

Finally, in order to model the problem of a growing tumour more realistically, we apply the theory in a novel manner to a problem on a growing domain, using a moving-boundary formulation of the problem. The growing tumour is modelled as a sphere of radius $R(t)$, where $R'(t)$ denotes the rate of growth of the tumour, assumed to be spherically symmetric (cf. [7, 8, 11] and references therein). The predictions of a linear stability analysis in this case indicate that as the tumour grows and the domain becomes larger, higher order modes should become excited. This in turn should lead to different spatial patterns appearing at different times. Numerical simulations carried out on the time-dependent domain $S(t)$, the surface of the sphere of radius $R(t)$, confirm this analysis, with different, higher order modes being excited as time increases and the domain becomes larger. This produces a series of "dynamic" pre-patterns of chemical concentrations which may, in turn, help to explain the clinically observed variation in cellular heterogeneity from cancer to cancer and individual to individual.

The layout of the paper is therefore as follows. In Section 2 we give a brief description of the linear stability analysis as applied to Turing-type reaction-diffusion systems. In Section 3 we present our (approximate) numerical scheme for the system (1.1) and our strategy for computing the reaction kinetics. In Section 4 we test the numerical scheme on a particular reaction-diffusion system with specific kinetics (Schnakenberg kinetics) and we show that the numerical results coincide with the theoretical predictions in this case. In Section 5, we describe the novel application of equations (1.2) to the modelling of a solid spherical tumour (of fixed size) just before invasion of its surrounding tissue occurs. We then apply the theory and the numerical method to the case of a growing domain and simulate the actual growth of a solid spherical tumour. Concluding remarks are made in the discussion section and finally in an appendix we present a brief error analysis for our numerical method.

2. Linearised stability theory

The reaction kinetics governing a general reaction-diffusion system may either be a pure or cross activator-inhibitor mechanism [18,48]. The distinction between these two types of kinetics lies in whether the self-activating chemical (cf. [78]) either activates (pure) or inhibits (cross) the second species. There is experimental evidence which suggests both mechanisms may be applicable in the case of growth factors secreted by tumour cells (cf. [10,17,64], [22,50,57,68]). For illustrative purposes only, here we assume that the kinetics are a cross activator-inhibitor mechanism, and we denote the concentration of the two chemical species by u and v.

For (1.2) in general, a homogeneous steady state is defined to be a pair $(u_0, v_0) \in \mathbb{R}^2$ such that

$$f(u_0, v_0) = g(u_0, v_0) = 0. \tag{2.1}$$

In linear stability analysis, (1.2) is said to exhibit "diffusion driven instability" if (u_0, v_0) is a linearly stable solution of (1.2) when diffusion is neglected, but unstable otherwise. The ranges of values of the parameters γ and d for which such a phenomenon can arise (the so called "Turing space") can be found in [49, p 387]. In the particular case under consideration in this paper, due to the spherical geometry, the eigenfunctions of the diffusion operator $\Delta_\star$ can be chosen as the spherical harmonics:

$$\begin{aligned} Y_n^m(\mathbf{x}) &= c_n^m P_n^{|m|}(\cos\theta)\exp(im\phi), \quad (\theta,\phi) \in [0,\pi] \times [0, 2\pi], \\ n &= 0, 1, 2, \ldots, |m| \le n, \end{aligned} \tag{2.2}$$

where $\mathbf{x} = \sigma(\theta,\phi) := (\sin\theta\cos\phi, \sin\theta\sin\phi, \cos\theta) \in S$, P_n^m are the Associated Legendre functions and c_n^m is chosen to be the normalising factor: $c_n^m = \sqrt{\frac{2n+1}{4\pi}\frac{(n-|m|)!}{(n+|m|)!}}$. It is well known that

$$\Delta_* Y_n^m = -k^2 Y_n^m, \tag{2.3}$$

where $k^2 = n(n+1)$. These properties of Δ_* can be combined with the general stability theory in [49, §14.3] where, in particular, it is shown that diffusion-driven instability can occur in (1.2), provided the values of the partial derivatives of f and g evaluated at (u_0, v_0) satisfy the inequalities

$$\begin{aligned} f_u + g_v &< 0, \quad |A| > 0, \\ df_u + g_v &> 0, \quad (df_u + g_v)^2 - 4d|A| > 0, \end{aligned} \tag{2.4}$$

with A denoting the Jacobian matrix, that is $A = \begin{bmatrix} f_u & f_v \\ g_u & g_v \end{bmatrix}$. These inequalities give a range of values of d for which instability may occur and the unstable modes are the spherical harmonics (2.2) with $|m| \le n$, provided n lies in the range

$$\gamma L(f_u, f_v, g_u, g_v, d) < k^2 = n(n+1) < \gamma M(f_u, f_v, g_u, g_v, d) \tag{2.5}$$

where

$$L = \frac{[df_u + g_v] - \{[df_u + g_v]^2 - 4d|A|\}^{1/2}}{2d}, \tag{2.6}$$

and

$$M = \frac{[df_u + g_v] + \{[df_u + g_v]^2 - 4d|A|\}^{1/2}}{2d}. \tag{2.7}$$

So, if there exists at least one n satisfying (2.5), then there is a possibility that a trajectory starting from a random perturbation of (u_0, v_0) will evolve into a spatially heterogeneous pattern generated by the spherical harmonics Y_n^m , $|m| \leq n$.

The above arguments are the main source of many results concerning spatial pattern formation over recent years, see, for example, [12], [49]. For the purpose of testing this theory it is useful to note that we can isolate a specific mode for "excitation" by choosing the parameters γ and d so that the width of the interval $[\gamma L, \gamma M]$ is sufficiently narrow so that (2.5) is satisfied for a unique n. Then the corresponding spherical harmonics are isolated unstable modes. We shall return to this in §4.

Following [12] we can apply this theory to case of the interaction of two chemicals on the surface of a solid spherical tumour. As stated previously, we assume that the reaction kinetics are of a cross activator-inhibitor mechanism, that is to say, regions of high concentration of the activator (or growth promoting factor, GPF) correspond to regions of low concentration of the inhibitor (or growth inhibitory factor, GIF) and vice versa [18]. Under the assumption that the growth factors are produced only by the live cells at the surface of the tumour, then the problem is essentially a 2-dimensional one on the spherical surface. The eigenfunctions are simply the surface harmonics Y_n^m and the wavenumbers in this case are given by $k^2 = n(n+1)$. Illustrations of the application of this linear stability analysis are given in [12].

Although this theory is not rigorous, it is widely known to produce results which are consistent with applications ([12, 48, 49]). Its main disadvantage is that it depends on analytic techniques and thus is restricted to reasonably simple domains and tractable kinetics. Numerical simulations, on the other hand, are much more generally applicable and so we now introduce our numerical method for simulating (1.1).

3. The spectral method of lines

We shall describe our numerical method in the context of the general evolution system (1.1). For integer $N \geq 1$, we let χ_N denote the space of spherical harmonics of degree $<N$ defined on the unit sphere S. An orthonormal basis for χ_N is

$$\{Y_n^m : 0 \leq |m| \leq n, \quad n = 0, \ldots, N-1\}, \tag{3.1}$$

and so $\dim \chi_N = N^2$. (Here orthonormality is with respect to the usual L_2 inner product on S, that is, $(v, w) = \int_S v\overline{w}$ and $\|v\|_{L_2} = (v, v)^{1/2}$.)

The solution $\mathbf{u}$ of (1.1) is a vector valued function $\mathbf{u} : S \times [0, \infty) \to \mathbb{R}^s$. Let L_2 denote the space of square integrable functions on S, and let $(L_2)^s$ and $(\chi_N)^s$ denote the $s-$fold Cartesian products of L_2 and χ_N. To approximate (1.1) in $(\chi_N)^s$, introduce the inner product on $(L_2)^s$:

$$(\mathbf{u}, \mathbf{v}) = \sum_{i=1}^{s} (u_i, v_i). \tag{3.2}$$

For $i = 1, \ldots, s$ let $\mathbf{e}_i$ denote the ith standard basis vector in $\mathbb{R}^s$. Then the set

$$\{Y_n^m \mathbf{e}_i, \quad i = 1, \ldots, s, \quad |m| \le n, \quad n = 0, \ldots, N-1\},$$

is an orthonormal basis for $(\chi_N)^s$. As is usual in the method of lines we approximate $\mathbf{u}(\mathbf{x}, t)$ in (1.1) by

$$\mathbf{u}_N(\mathbf{x}, t) := \sum_{n=0}^{N-1} \sum_{|m| \le n} \mathbf{U}_n^m(t) Y_n^m(\mathbf{x}), \tag{3.3}$$

where $\mathbf{U}_n^m : [0, \infty) \to \mathbb{R}^s$. Equivalently,

$$\mathbf{u}_N(\mathbf{x}, t) = \sum_{i=1}^{s} \sum_{n=0}^{N-1} \sum_{|m| \le n} (\mathbf{U}_n^m)_i(t) Y_n^m(\mathbf{x}) \mathbf{e}_i. \tag{3.4}$$

A standard method for determining the unknown time-dependent coefficients $\mathbf{U}_n^m(t) \in \mathbb{R}^s$ is to apply the *Galerkin method* in space to (1.1), that is, to require that

$$((\mathbf{u}_N)_t, \mathbf{v}_N) = (D\Delta_* \mathbf{u}_N, \mathbf{v}_N) + (\mathbf{f}(\mathbf{u}_N), \mathbf{v}_N) \tag{3.5}$$

for all $\mathbf{v}_N \in (\chi_N)^s$. An equivalent statement is to require that (3.5) holds for all $\mathbf{v}_N$ of the form $\mathbf{v}_N = Y_{\tilde{n}}^{\tilde{m}} \mathbf{e}_j, \quad j = 1, \ldots, s; \quad |\tilde{m}| \le \tilde{n}; \quad \tilde{n} = 0, \ldots, N-1$, which, using (2.3), is equivalent to the sN^2-dimensional nonlinear system of odes:

$$\begin{aligned} \left(\mathbf{U}_{\tilde{n}}^{\tilde{m}}\right)_j' &= -d_j \tilde{n}(\tilde{n}+1) \left(\mathbf{U}_{\tilde{n}}^{\tilde{m}}\right)_j + \left(f_j(\mathbf{u}_N), Y_{\tilde{n}}^{\tilde{m}}\right), \\ j &= 1, \ldots, s, \ |\tilde{m}| \le \tilde{n}, \ \ \tilde{n} = 0, \ldots, N-1. \end{aligned} \tag{3.6}$$

In the method of lines approach, (3.6) is solved using a (stiff) ode solver to return the solution to appropriate tolerance. This is a standard method and will work well provided we have an efficient method for computing the quantities

$$(f_j(\mathbf{u}_N), Y_{\tilde{n}}^{\tilde{m}}) \tag{3.7}$$

appearing on the right hand side of (3.6).

Since $\mathbf{u}_N$ is given by (3.4) and since the Y_n^m are orthonormal, (3.7) is trivial to compute if $\mathbf{f}$ is an affine map on $\mathbb{R}^s$. In the nonlinear case which we are interested in here, this computation is no longer trivial. In the special case when $f_j(\mathbf{u})$ is a low order polynomial in $\mathbf{u}$, there are reasonable ways of computing (3.7) analytically using spherical harmonic expansions of products of spherical harmonics (for example, using "Wigner symbols" as discussed in [19]). Although higher order polynomials can in principle be handled by iterating this approach, in practice this leads to ever more complex analytic formulae and does not generalise to the case when $\mathbf{f}$ is non-polynomial.

Instead we propose a more general method by computing (3.7) using a suitable quadrature rule. The resulting method is then fully discrete and can be applied without increased complexity to any nonlinear map $\mathbf{f}$. Moreover, as we shall see in the Appendix, under reasonable assumptions the resulting fully discrete method has the same exponential convergence rate as $N \to \infty$, as can be proved for the true Galerkin scheme (3.5) for linear model problems, and so there is no *a priori* disadvantage in the replacement of (3.7) by a suitably accurate quadrature expansion.

Our quadrature scheme for (3.7) is based on the following standard rule:

$$\int_S \psi \approx \frac{2\pi}{M} \sum_{q=1}^{M} \sum_{p=1}^{M/2} w_p \psi(\sigma(\theta_p, \phi_q)), \tag{3.8}$$

where $M \geq 2$ is an even integer, w_p, and $\cos\theta_p, \quad p = 1, \ldots, M/2$ are the Gauss-Legendre weights and nodes on $[-1, 1]$ and $\phi_q = 2q\pi/M, \quad q = 1, \ldots, M$. The rule (3.8) requires $M^2/2$ evaluations of ψ and is exact when ψ is a polynomial of degree $M-2$ on S (see, for example, [65, p. 41]). Using (3.8), we define a discrete inner product

$$(u, v)_M = \frac{2\pi}{M} \sum_{q=1}^{M} \sum_{p=1}^{M/2} w_p u(\sigma(\theta_p, \phi_q)) \overline{v}(\sigma(\theta_p, \phi_q)) \tag{3.9}$$

which is well-defined for continuous u, v. From this we build the corresponding discrete version of (3.2):

$$(\mathbf{u}, \mathbf{v})_M := \sum_{i=1}^{s} (u_i, v_i)_M, \tag{3.10}$$

which leads to the discrete Galerkin method for (1.1):

$$((\mathbf{u}_N)_t, \mathbf{v}_N) = (D\Delta_* \mathbf{u}_N, \mathbf{v}_N) + (\mathbf{f}(\mathbf{u}_N), \mathbf{v}_N)_M \tag{3.11}$$

and yields (instead of (3.6)), the fully discrete sN^2-dimensional nonlinear system of odes:

$$\begin{aligned} \left(\mathbf{U}_{\tilde{n}}^{\tilde{m}}\right)'_j &= -d_j \tilde{n}(\tilde{n}+1) \left(\mathbf{U}_{\tilde{n}}^{\tilde{m}}\right)_j + \left(f_j(\mathbf{u}_N), Y_{\tilde{n}}^{\tilde{m}}\right)_M, \\ j &= 1, \ldots, s, \ |\tilde{m}| \leq \tilde{n}, \ \ \tilde{n} = 0, \ldots, N-1. \end{aligned} \tag{3.12}$$

We shall see in the Appendix that M should grow modestly with N in order to preserve the accuracy of the method (3.11). In particular if $\mathbf{f}$ is a polynomial (as is the case in our applications in §§4,5), then $M = O(N)$ will suffice. The efficient solution of (3.11) using a suitable stiff ODE solver (in our experiments the MATLAB ODE15s) then requires the fast computation at each time t of the discrete inner products

$$\left(f_j(\mathbf{u}_N), Y_{\tilde{m}}^{\tilde{n}}\right)_M = \frac{2\pi}{M} \sum_{q=1}^{M} \sum_{p=1}^{M/2} w_p f_j(\mathbf{u}_N(\sigma(\theta_p, \phi_q), t)) \overline{Y_{\tilde{m}}^{\tilde{n}}}(\sigma(\theta_p, \phi_q)), \tag{3.13}$$

for each $\tilde{n}, \tilde{m}$ and j, under the assumption that the coefficients $(U_n^m)_i$ in (3.4) are given. This requires essentially three steps.

- *Step 1.* Evaluation of the right-hand side of (3.4) at $\mathbf{x} = \sigma(\theta_p, \phi_q)$ for each $p = 1, \ldots, M/2, q = 1, \ldots, M$, hence obtaining $\mathbf{u}_N(\sigma(\theta_p, \phi_q), t)$.
- *Step 2.* Evaluation of $f_j(\mathbf{u}_N(\sigma(\theta_p, \phi_q), t))$ for each $j = 1, \ldots, s,\ p = 1, \ldots, M/2,\ q = 1, \ldots, M$.
- *Step 3.* Computation of (3.13) for each $\tilde{n}, \tilde{m}$ and j.

To examine the complexity of this computation as N increases, let us assume (as mentioned above) that $M = O(N)$ and s is fixed. Since $\mathbf{f}$ is a given function independent of N and M, each evaluation of f costs $O(1)$ operations and Step 2 costs $O(M^2) = O(N^2)$ operations. Direct implementation of each of Steps 1 and 3 costs $O(N^4)$ operations but fortunately this can be reduced by exploiting the structure of these sums. Considering Step 1 first, the simplest reduction is obtained by combining (2.2) and (3.3) to obtain

$$\mathbf{u}_N(\sigma(\theta_p, \phi_q), t) = \sum_{n=0}^{N-1} \left\{ \sum_{|m| \le n} \mathbf{U}_n^m(t)\ c_n^m\ P_n^{|m|}(\cos\theta_p)\ \exp(im\phi_q) \right\}.$$

The inner sums can be computed simultaneously for $q \in \{1, \ldots, N\}$ in $O(N \log N)$ operations using FFT. There are N terms in the outer sum and the result must be computed for each p, resulting in $O(N^3 \log N)$ operations. Using an analogous decomposition of (3.13), the sum over q can be handled similarly so that the total complexity of Step 3 can also be reduced to $O(N^3 \log N)$. This is the method used in the present work and it returns quite reasonable computation times, as we shall see. Since approximation with spherical harmonics is exponentially convergent, we shall see that values of N considerably less than about 20 are often sufficient to obtain the required spatial accuracy. We note however the very interesting recent Ph.D. thesis [42] which obtains a method for Steps 1 and 3 which are asymptotically faster than $O(N^3)$ and can even achieve $O(N^2 \log^2 N)$. However this method is faster than the simple FFT method discussed above only for considerably higher values of N than those used and required in our numerical method. So we do not employ these more sophisticated techniques here.

4. Numerical experiments on the Schnakenberg system

In this section, we demonstrate the effectiveness of our numerical scheme in the particular case of the Schnakenberg system on $S \times [0, \infty)$:

$$u_t = \Delta_* u + \gamma f(u, v) = \Delta_* u + \gamma(a - u + u^2 v), \tag{4.1}$$

$$v_t = d\Delta_* v + \gamma g(u, v) = d\Delta_* v + \gamma(b - u^2 v), \tag{4.2}$$

where a, b, d, γ are all positive parameters. For all $d, \gamma > 0$ the positive spatially homogeneous steady state (u_0, v_0) is given by:

$$u_0(\mathbf{x}) = u_0 = a + b\ , \quad v_0(\mathbf{x}) = v_0 = \frac{b}{(a+b)^2}\ , \quad \mathbf{x} \in S. \tag{4.3}$$

At the steady state (u_0, v_0), we then have

$$f_u = (b-a)/(b+a), \quad f_v = (a+b)^2 = -g_v, \quad g_u = -2b/(a+b)\ . \tag{4.4}$$

Applying the linearised stability theory outlined in §2 to this case shows that, if $b > a$, then there exist wavenumbers $k^2 = n(n+1)$ such that the corresponding spherical harmonics Y_n^m, $|m| \leq n$ are unstable modes of (4.1)-(4.2) (linearised about (4.3)), provided

$$\gamma L < k^2 < \gamma M \,, \tag{4.5}$$

where

$$L = \frac{\left[d(b-a) - (a+b)^3\right] - \{\left[d(b-a) - (a+b)^3\right]^2 - 4d(a+b)^4\}^{1/2}}{2d(a+b)} \,, \tag{4.6}$$

and

$$M = \frac{\left[d(b-a) - (a+b)^3\right] + \{\left[d(b-a) - (a+b)^3\right]^2 - 4d(a+b)^4\}^{1/2}}{2d(a+b)} \,. \tag{4.7}$$

In this section we validate our numerical method by showing that it is consistent with the linearised stability theory for (4.1)-(4.2).

In order to focus our numerical experiments we first note that in the linearised theory, we can select a specific unstable wavenumber k^2 to "excite" by choosing γ so that the width of the interval $[\gamma L, \gamma M]$ in (4.5) is centred on k^2 and narrow enough to contain only that wavenumber. Then we may expect that the eventual inhomogeneous steady state will be rich in the modes Y_n^m , $|m| \leq n$ for that particular value of n. More precisely, it is shown in [49, p. 384] that for fixed a, b with $b > a$, there is a critical value of d, namely

$$d_c = \frac{(f_u g_v - 2 f_v g_u) + \sqrt{(f_u g_v - 2 f_v g_u)^2 - f_u^2 g_v^2}}{f_u^2} \,, \tag{4.8}$$

with f_u, g_u, f_v and g_v given by (4.4), for which unstable modes are possible if and only if $d > d_c$. Moreover when $d > d_c$ and d is sufficiently close to d_c, then by setting

$$\gamma = \gamma_c = \frac{2 d_c \tilde{k}^2}{d_c f_u + g_v} = \frac{2 d_c \tilde{k}^2}{d_c (b-a)/(b+a) - (a+b)^2} \,, \tag{4.9}$$

for any chosen $\tilde{k}^2$, we can ensure that (4.5) contains the single wavenumber $\tilde{k}^2$. This gives a convenient class of problems which can be used to compare numerical simulations with the results predicted by linearised stability theory. In all of our numerical experiments we set

$$a = 0.2, \quad \text{and} \quad b = 1,$$

which, from (4.3), yields values of $u_0 = 1.2$ and $v_0 = 0.69$. We note that the above choice of values for the parameters a and b is (in the absence of any experimental data) arbitrary. However, these values then enable us to calculate the critical value of d, which from (4.8) yields $d_c = 17.0056$. Choosing d just greater than d_c and an appropriate value of γ from (4.9) then provides us with a set of parameter values which can be expected to ensure the existence of unstable modes and hence spatially heterogeneous steady states.

We approximate the solution $(u, v)^T$ of (4.1)–(4.2) using the method of lines outlined in §3. With a slight abuse of the notation in §3, we express the numerical solution as

$$u_N(\mathbf{x}, t) = \sum_{n=0}^{N-1} \sum_{m=-n}^{n} U_n^m(t) Y_n^m(\mathbf{x}), \qquad v_N(\mathbf{x}, t) = \sum_{n=0}^{N-1} \sum_{m=-n}^{n} V_n^m(t) Y_n^m(\mathbf{x}). \tag{4.10}$$

For convenience we shall order the basis of χ_N as $Y_0^0, Y_1^{-1}, Y_1^0, Y_1^1, \ldots, Y_{N-1}^{N-2}, Y_{N-1}^{N-1}$. The coefficients of these functions in (4.10) are vectors with N^2 components which we write as $\mathbf{U}(t), \mathbf{V}(t) \in \mathbb{R}^{N^2}$, with the corresponding ordering, that is, $\mathbf{U}(t) = (U_1(t), U_2(t), \ldots, U_{N^2}(t))$ where $U_1(t)$ is the coefficient of Y_0^0 and so on. We use this notation in some of the figures below.

In the following four experiments, unless specified, we took $N = 8$, so that the system of ODEs (corresponding to (3.12)) has dimension $2N^2 = 128$. In this case we set $tol = 10^{-4}$, where tol is the applied tolerance for the ODE solver used to integrate (3.6). This is one of a family of parameter choices which we shall refer to later in (4.12). Because the Schnakenberg kinetics are polynomials of degree ≤ 3 in (u, v), we chose $M = 4N$ in the quadrature rule (3.8). In the Appendix this choice is shown to be sufficent for superalgebraic convergence of the method. When integrating the ODE system arising from the method of lines, we define a steady state to have been reached at time t_f if, for each j, the absolute value of the difference between successive values of $U_j(t)$ at $t = t_f - \tau$ is less than 10^{-8} for $\tau = 0, 0.2, 0.4., 0.6, 0.8$, with an identical check on $V_j(t)$. We checked this criterion at time intervals of length 10 and stopped when it was satisfied.

In Experiments 1–4 below, the initial conditions which we took consisted of small random perturbations of the order of 10^{-4} of the homogeneous steady state $(u_0, v_0) = (1.2, 0.69)$, that is

$$\left.\begin{aligned} u_N(\mathbf{x}, 0) &= u_0 + \textstyle\sum_{n=0}^{N-1} \sum_{m=-n}^{n} U_n^m(0) Y_n^m(\mathbf{x}), \\ v_N(\mathbf{x}, 0) &= v_0 + \textstyle\sum_{n=0}^{N-1} \sum_{m=-n}^{n} V_n^m(0) Y_n^m(\mathbf{x}), \end{aligned}\right\} \tag{4.11}$$

where $|U_n^m(0)| \leq 10^{-4}$ and $|V_n^m(0)| \leq 10^{-4}$ for all $n = 0, \ldots, N-1$ and $|m| \leq n$. A typical set of the 64 coefficients $(U_1(0), U_2(0), \ldots, U_{64}(0))$ used as an initial perturbation is shown in Figure 4.1.

Note that throughout the paper we choose the perturbation coefficients $U_n^m(0)$, $V_n^m(0)$ to be real and to satisfy the symmetry relations $U_n^m = \overline{U_n^{-m}}$ and $V_n^m = \overline{V_n^{-m}}$ for all $1 \leq |m| \leq n$. This ensures that the initial conditions $u_N(\mathbf{x}, 0)$ and $v_N(\mathbf{x}, 0)$ are real-valued functions. The imaginary parts of $u_N(\mathbf{x}, t)$ and $v_N(\mathbf{x}, t)$ in (4.10) then remain negligible (of the order of 10^{-9}) throughout the integration of the ODE system arising from the method of lines (3.6) applied to (4.1), (4.2).

Experiment 1. In the first experiment we studied excitation of the modes of degree $n = 2$ (wavenumber $k^2 = 6$), comprising span$\{Y_2^m : |m| \leq 2\}$. First we set $d = 15 < d_c$ and chose $\gamma = \gamma_c$ as in (4.9) with $\tilde{k}^2 = 6$. For several different

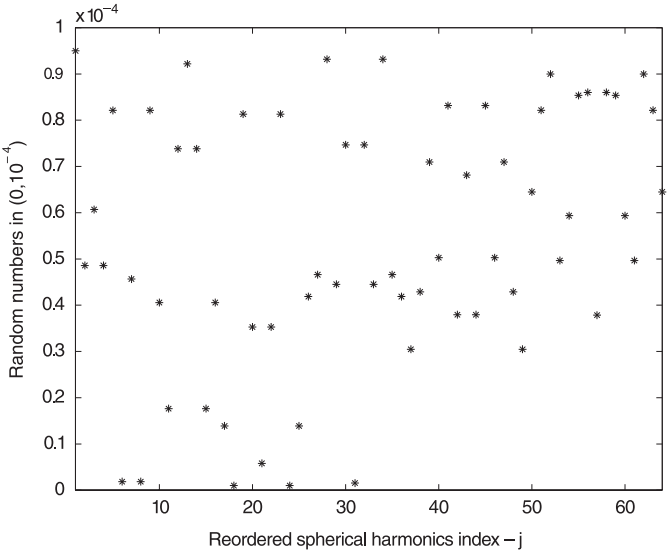

Fig. 4.1. Figure showing the values of the components $U_j(0)$, $j = 1, \ldots, 64$ used in the initial conditions as a small random perturbation of u_0.

sets of small randomly perturbed initial conditions, the numerical method obtained (u_0, v_0) as the resultant steady state, thus demonstrating its stability in this case, as predicted by the linear stability analysis.

Next we set $d = 18 > d_c$ and $\gamma = \gamma_c$, again with $\tilde{k}^2 = 6$. In this case then $k^2 = 6$ is the only wavenumber satisfying (4.5) and so we expect the resulting steady state to be rich in the corresponding modes of degree 2. With the ordering described above, the components of u_N and v_N in the direction of these modes are $U_j(t)$, $V_j(t)$ for $j = 5, 6, 7, 8, 9$. An interesting question was whether the excitement was only around these indices as a steady state evolves. In fact, our numerical experiments show this exactly to be the case. Figure 4.2 shows the plots of the precise components which are excited at various times during the numerical simulation. As we see from the results of Figure 4.2, no substantial excitement happens until about time $t = 15$, but begins to occur in the components $j = 5, 6, 7, 8, 9$ and becomes more substantial at about $t = 20$. (Note that the homogeneous steady state itself is composed completely of the constant mode $j = 0$.) These remain the dominant modes of excitement until an inhomogeneous steady state is reached, at about $t = 50$.

Plots of the corresponding spatially heterogeneous steady states $u_8(\mathbf{x}, 50)$ and $v_8(\mathbf{x}, 50)$ are given in Figure 4.3. These plots show the predicted heterogeneous concentration distributions of each chemical u and v on the surface of the sphere obtained from the excited modes of Figure 4.2. Note that regions of high u values correspond to regions of low v values and vice versa.

To demonstrate that the features of $u_8(\mathbf{x}, 50)$ and $v_8(\mathbf{x}, 50)$ are not artifacts of our numerical method we first added a small random perturbation to $u_8(\mathbf{x}, 50)$

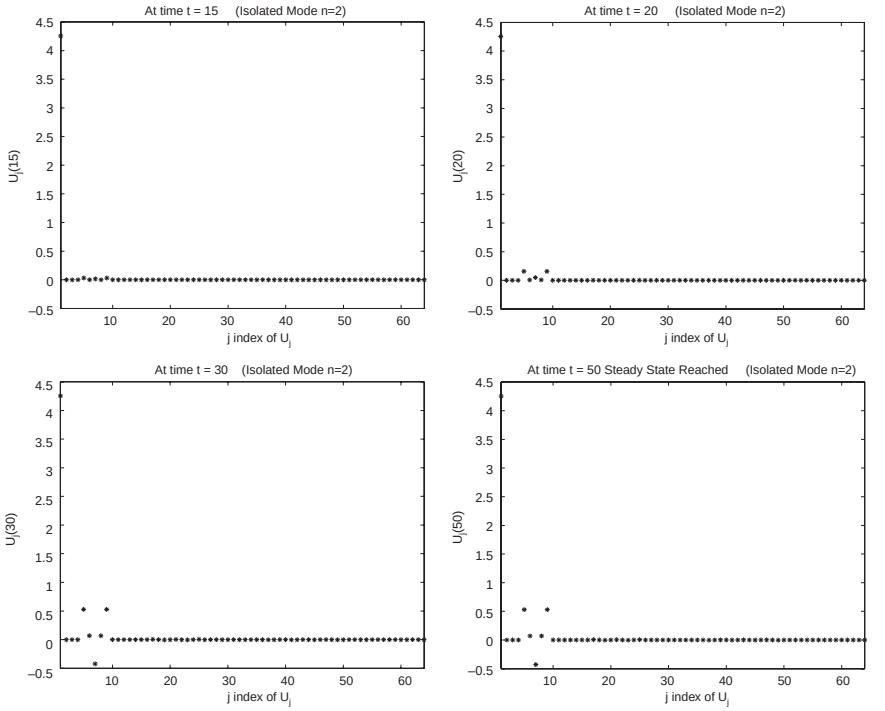

Fig. 4.2. *Experiment 1.* Results from a numerical experiment attempting specific excitation of the $n = 2$ modes corresponding to the functions Y_2^m. The graphs show the values of the coefficients $U_j(t)$, plotted against j, $j = 1, \ldots, 64$ for each spherical harmonic at times $t = 15, 20, 30$ and 50 (reading consecutively from top left to bottom right). The ordering of the components $U_j(t)$ and their associated spherical harmonic Y_n^m is as per section 4. The figure shows excitation of the components $U_5(t), \ldots, U_9(t)$ corresponding to the spherical harmonics Y_2^m as predicted by the linear stability analysis.

and $v_8(\mathbf{x}, 50)$ and then restarted the ODE solver. The result was that we recovered $(u_8(\mathbf{x}, 50), v_8(\mathbf{x}, 50))$ back again as the steady state, demonstrating its stability.

To check the accuracy of our results, we repeated the experiment with the parameters chosen as

$$N = 4K\ , \quad M = 4N\ , \quad tol = 10^{-2K}\ , \quad K = 2, 3, 4 \tag{4.12}$$

where tol is the applied tolerance of the ODE solver for (3.6). The initial condition was chosen to be the same random perturbation (4.11) in each case. Let $u_{4K} = u_{4K}(\mathbf{x}, t)$ denote the corresponding method of lines solutions. Choosing u_{16} as the "exact" solution and then computing the approximate errors:

$$e_K(t) = \|u_{4K}(\cdot, t) - u_{16}(\cdot, t)\|_{L_2}\ , \quad K = 2, 3, \tag{4.13}$$

we obtain the results:

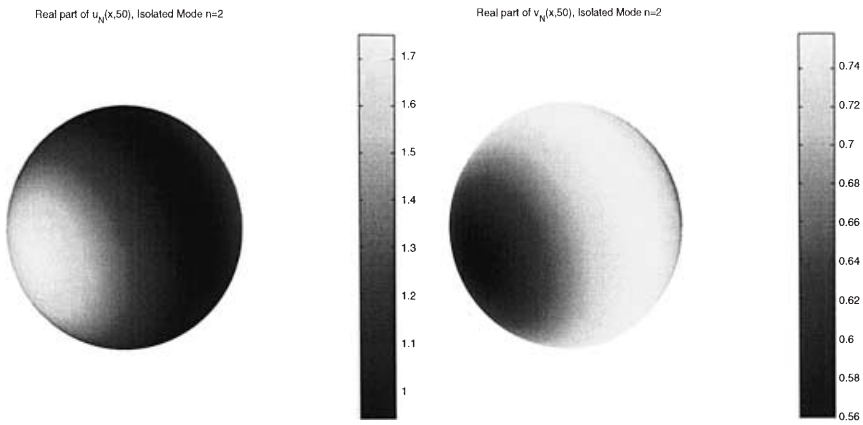

Fig. 4.3. *Experiment 1.* Final steady state distributions of the chemical concentration profiles $u_8(.,50)$ and $v_8(.,50)$ over the surface of the sphere (mode $n = 2$ excitation).

Table 1. Errors obtained from the accuracy test for Experiment 1, calculated from (4.13).

t	$e_2(t)$	$e_3(t)$
10	1.75e-03	6.06e-04
20	7.95e-02	1.52e-02
30	2.05e-02	6.23e-03
40	6.85e-03	6.79e-04
50	6.85e-03	6.79e-04

The results in Table 1 suggest that the case $K = 2$ (leading to $N = 8$) which is used to produce Figures 4.2, 4.3 is accurate to about 2 decimal places and certainly accurate enough to guarantee the validity of these figures.

Experiment 2. Here we studied excitation of the modes of degree $n = 4$, comprising the 9 dimensional space span$\{Y_4^m : |m| \leq 4\}$, and corresponding to the wavenumber $k^2 = 20$. As before we chose $d = 18 > d_c$ and $\gamma = \gamma_c$ given by (4.9) with $\tilde{k}^2 = 20$. Then $k^2 = 20$ is the only wavenumber satisfying the inequality (4.5). Here we expected the dominant deviation from the homogeneous steady state to occur in the components $U_j(t)$, $V_j(t)$ for $j = 17, 18, \ldots, 24, 25$. This was essentially the case, with the steady state solution (reached at time $t = 20$, with initial excitement occuring at time $t = 5$) being composed mainly of contributions from each of the modes Y_4^m, $|m| \leq 4$. The actual steady state pre-patterns of the concentrations of the two chemicals $u_8(\mathbf{x}, 20)$, $v_8(\mathbf{x}, 20)$ on the surface of the sphere are depicted in Figure 4.4. □

Experiment 3. Here we proceed analogously to the previous two experiments, but this time we study excitation of modes of degree 6, namely Y_6^m, $|m| \leq 6$. Because in this case we expect that employing $N = 8$ in the method of lines may not be sufficient for spatial accuracy, we employ $N = 12$ (corresponding to the case $K = 3$ in (4.12)). We present only the plots of the resulting steady state chemical concentration profiles of u_{12}, v_{12} on the surface of the sphere (Figure 4.5). As a

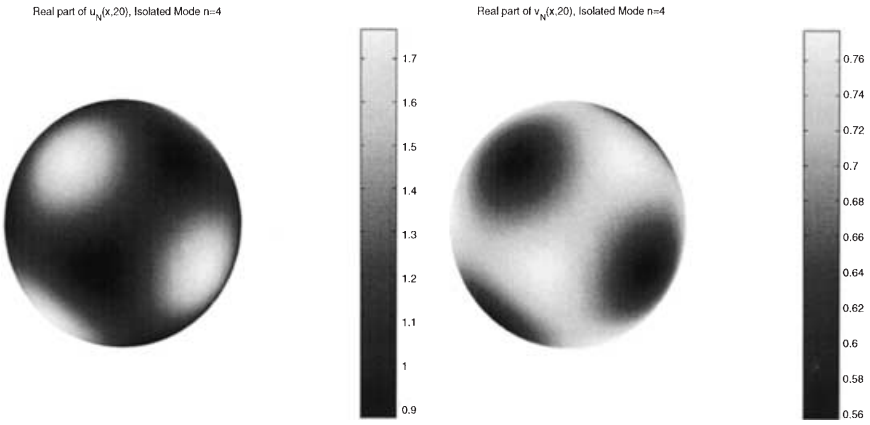

Fig. 4.4. *Experiment 2.* Final steady state distributions of the chemical concentration profiles $u_8(., 20)$ and $v_8(., 20)$ over the surface of the sphere (mode $n = 4$ excitation).

check on accuracy we repeated the experiment with $N = 16$ and found graphically identical results (Figure 4.6).

Experiment 4. Finally we present numerical simulations for the Schnakenberg system where the linear stability analysis predicts no particular dominant mode and so the expected heterogeneous steady state pattern should have no particular symmetry. For this purpose, we chose $d = 25$ and $\gamma = 100$. Figure 4.7 shows the particular modes excited at various times during the numerical simulation. In this case, the steady state is reached at time $t = 40$ and, as we see in Figure 4.7, excitement begins as early as time $t = 3$ and no particular mode dominates throughout. The computed steady states $u_{12}(\mathbf{x}, 40)$, $v_{12}(\mathbf{x}, 40)$ have contributions from all modes in the numerical model. We checked the accuracy of our results as in Experiment 1. Figure 4.8 shows the plots of the concentrations of the steady state distributions of u_{12}, v_{12} on the surface of the sphere. Although once again a spatially heterogeneous steady state has been reached (with regions of high and low concentrations of each chemical), no particular mode dominates, and the resulting pattern contains no obvious symmetry.

The above results of our numerical experiments confirm the predictions of the linear stability analysis and verify the accuracy and stability of the numerical method. In the next section we apply our method to an actual biological problem – that of modelling solid tumour growth – and explore the possible rôle that pre-pattern theory may play in this process.

5. The rôle of pre-pattern theory in tumour growth and invasion

5.1. Application to a spherical tumour

In vivo cancer growth, and as a particular example in this paper, solid tumour growth (for example, a carcinoma, or cancer of the epithelial tissue) is a complicated

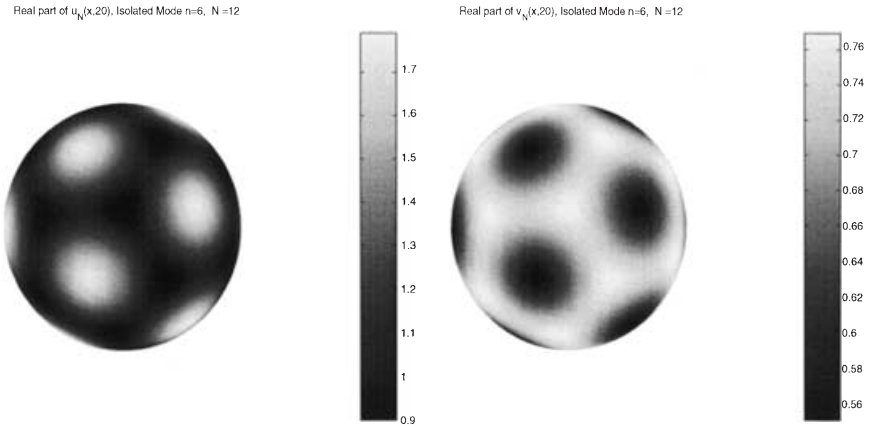

Fig. 4.5. *Experiment 3 (with N=12).* Final steady state distributions of the chemical concentration profiles $u_{12}(., 20)$ and $v_{12}(., 20)$ over the surface of the sphere (mode $n = 6$ excitation).

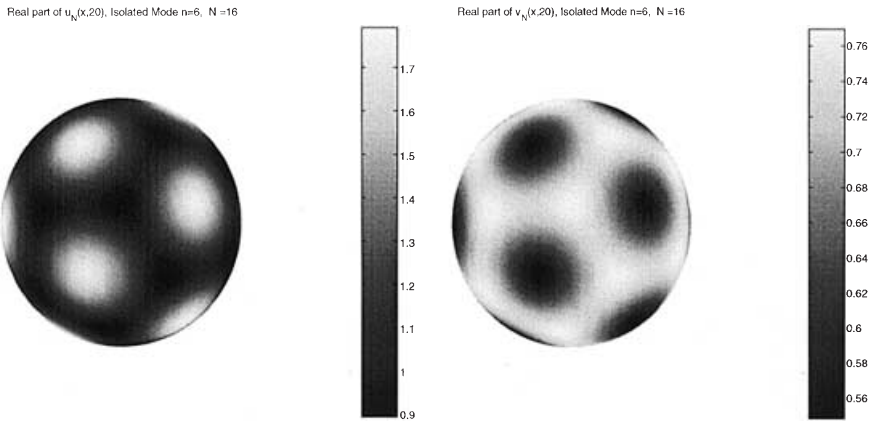

Fig. 4.6. *Experiment 3 (with N=16).* Final steady state distributions of the chemical concentration profiles $u_{16}(., 20)$ and $v_{16}(., 20)$ over the surface of the sphere (mode $n = 6$ excitation). Figures 4.5 and 4.6 demonstrate the convergence of the numerical scheme.

phenomenon involving many inter-related nonlinear processes and, as such, presents the mathematical modeller with a correspondingly complex set of problems to solve. Even deciding which simplifying assumptions to make is a non-trivial task. It is now thought that all cancers begin with the (genetic) mutation of a single cell into a "transformed cell". Subsequent mutations lead to the so-called transformed cells escaping the body's normal growth control mechanisms. If the transformed cells can overcome any immune system attack then a small mass of proliferating cells may be formed – a nascent solid tumour. Solid tumours are known to progress through two distinct phases of growth – the avascular phase and the vascular phase. During

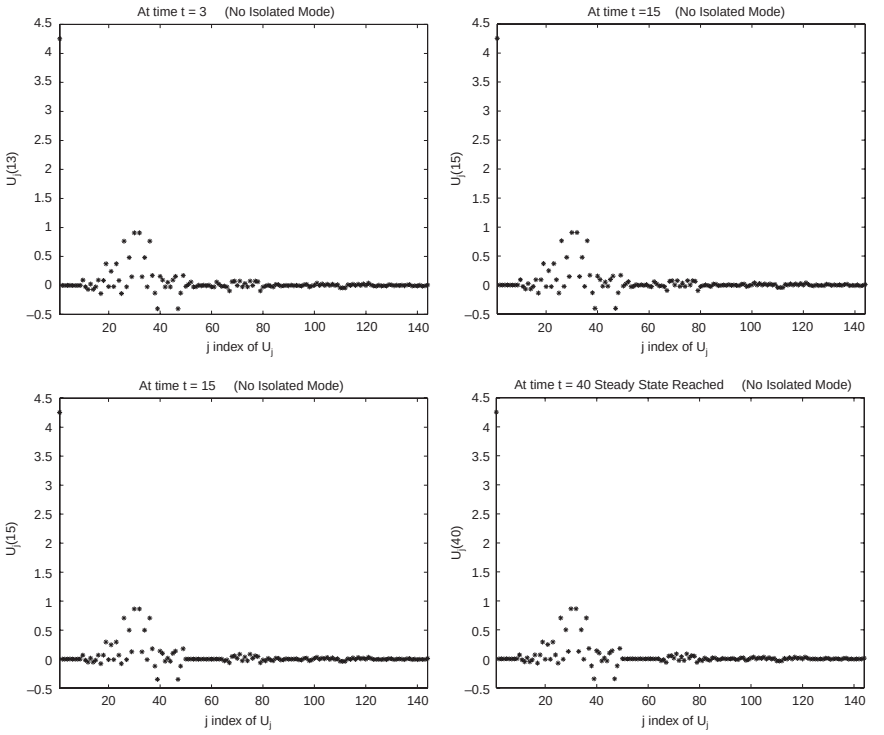

Fig. 4.7. *Experiment 4.* Results from a numerical experiment attempting no specific excitation of any particular mode. The graphs show the values of the coefficients $U_j(t)$, plotted against j, $j = 1, \ldots, 144$ for each spherical harmonic at times $t = 3, 15, 25$ and 40 (reading consecutively from top left to bottom right). The ordering of the components $U_j(t)$ and their associated spherical harmonic Y_n^m is as per section 4. The figure shows excitation of a range of components with no particular mode dominating as predicted by the linear stability analysis.

the former growth phase the tumour remains in a diffusion-limited, dormant state (cf. multicell spheroids, carcinoma *in situ*) while during the latter growth phase, invasion and metastasis may take place.

The initial avascular growth phase can be studied in the laboratory by culturing cancer cells in the form of three-dimensional *multicell spheroids* ([46, 67] and references therein). It is well known that these spheroids, whether grown from established tumour cell lines or actual *in vivo* tumour specimens, possess growth kinetics which are very similar to *in vivo* tumours. Typically, these avascular nodules may grow to a few millimetres in diameter depending on the cell types and the culture conditions used, although carcinoma *in vivo* may reach dormancy at a smaller size of between 250–500μm [46, 67]. Cells towards the centre of the spheroid, being deprived of vital nutrients, die and give rise to a necrotic core. Proliferating cells can be found in the outer three to five cell layers, that is, *essentially on the surface of the tumour*. Lying between these two regions is a layer of quiescent cells, a proportion of which can be recruited into the outer layer of proliferating cells.

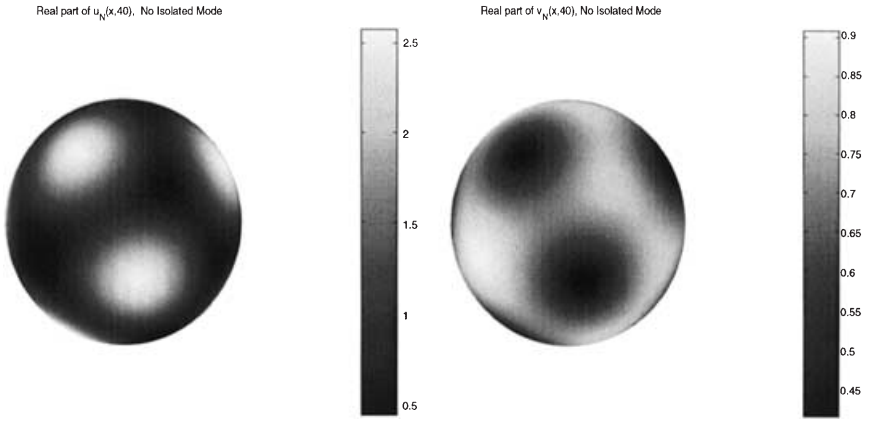

Fig. 4.8. *Experiment 4.* Final steady state distributions of the chemical concentration profiles $u_{12}(., 40)$ and $v_{12}(., 40)$ over the surface of the sphere, in the situation where no single mode is excited.

Much experimental data has been gathered on the internal architecture of spheroids, and studies regarding the distribution of vital nutrients (for example, oxygen) and metabolites within the spheroids have been carried out [24, 77].

The transition from the dormant avascular state to the vascular state, wherein the tumour possesses the ability to invade surrounding tissue and metastasise to distant parts of the body, depends upon its ability to induce new blood vessels from the surrounding tissue to sprout towards and then gradually penetrate the tumour, thus providing it with an adequate blood supply and micro-circulation and permitting vascular growth to take place. It is during this stage of growth that the insidious process of invasion takes place. Once vascularized, the tumours grow rapidly as exophytic masses. In certain types of cancer, for example, carcinomas arising within an organ, this process typically consists of columns of cells projecting from the central mass of cells and extending into the surrounding tissue area and the local spread of these carcinomas often assume an irregular jagged shape. We also note however, that not all tumours require vascularization to occur prior to invasion – in some tumours some amount of invasion is accomplished through the secretion of enzymes which degrade the local tissue (see [3] and references therein); in others, vascularization and invasion proceed simulatneously. By the time a tumour has grown to a size whereby it can be detected by clinical means, there is a strong likelihood that it has already reached the vascular growth phase.

Prior to successful completion of angiogenesis, the avascular tumour, although dormant (or quasi-dormant) with regard to its growth, is still very much in a "dynamic state of equilibrium", with cell birth and proliferation in balance with cell loss and death. Many previous mathematical models (for example, [7, 8, 11] and references therein) have modelled this avascular phase of growth by a spherical mass of tumour cells whose radially symmetric growth is governed by (i) the distribution of a vital nutrient such as oxygen and (ii) the distribution of a generic growth inhibitory factor, the existence and properties of chemicals which inhibit mitosis

being very well documented, for example, [34]. The growth inhibitory factor and nutrient distributions compete to control the tumour cell proliferation and therefore ultimately the size of the tumour.

However it is also known that tumour cells themselves secrete growth-promoting factors [53]. Reference [12] studied the evolution of the concentrations of both growth-inhibiting and growth-promoting factors governed by a system of reaction-diffusion equations on the surface and interior of a sphere. The predicted spatially heterogeneous steady-states of these two chemicals were shown to correspond to observed regions of cellular heterogeneity in actual solid tumours. The results presented in [12] were purely theoretical and depended entirely upon a linear stability analysis. In this section we once again consider the rôle that pre-pattern theory may play in the growth and invasion of tumours, but, in this case, we will extend and substantiate the work in [12]. In formulating our model we take into account the following observations:

- Experimental results have demonstrated that tumour cells secrete both growth-inhibiting and growth-activating chemicals in an autocrine manner [53] and that the balance and interaction between these factors play an important role in the development and progression of tumours [21, 45, 53, 54, 58].

Growth inhibitors:

- Transforming growth factor betas (TGF-βs) constitute a family of local mediators that regulate the proliferation and functions of many cell types. Indeed TGF-βs have an identified effect of specifically suppressing tumour cell proliferation in many types of cancers [1, 36, 44, 55, 79], including carcinomas.
- TGF-βs also are known to induce apoptosis (cell death) in carcinoma cells [79] and can stimulate the synthesis of the extracellular matrix and equally importantly the tumour stroma. They have therefore been implicated in controlling cancer invasion [2, 75].

Growth promoters:

- There is also much evidence to demonstrate that many types of tumour cells (including carcinoma cells) also secrete a variety of growth-promoting factors. For example, epidermal growth factor (EGF) and transforming growth factor-α (TGF-α) [80]; basic fibroblast growth factor (bFGF) [70]; platelet-derived growth factor (PDGF) [76]; insulin-like growth factor (IGF) [15] [54] [73]; interleukin-1α (IL-1α) [81] [33] and granulocyte colony-stimulating factor (G-CSF) [45].

Interestingly, and indeed perhaps somewhat paradoxically [38], tumour-necrosis-factor-α (TNF-α) has been identified as both a growth promoter (increasing the proliferation of tumour cells) [13, 64, 78] and also as a growth inhibitor (inhibiting cell proliferation) [52], [63]. The precise function of this cytokine appears to depend on the cell type it acts on and its concentration level.

- Not only can we identify specific growth inhibitors and activators (as opposed to generic chemicals), but there is direct experimental evidence that in tumour

cell lines these chemicals interact and modulate the effect of each other [10, 17, 22, 26, 39, 50, 57, 64, 68].

In addition to the above experimental observations, it is also well known that the timescale of a growing tumour (even a fast-growing, aggressive, invasive tumour) is very much slower than the diffusion timescale of chemicals. This fact has been exploited in almost all of the previous mathematical models for avascular tumour growth (cf. [7, 8, 11] and references therein). Any chemical which is produced by the tumour cells will therefore diffuse and reach a steady-state distribution within its domain on a much faster timescale than the growing tumour itself. We therefore consider the possibility of the development of a genuine heterogeneous chemical pre-pattern on the surface of a solid tumour which takes place prior to successful angiogenesis. This chemical pre-pattern predisposes cells in certain regions on the surface of the tumour (that is, in regions where the concentration of the growth-promoting factor is high) to invasion and subsequently facilitates the vascular, invasive growth. Such cellular heterogeneity in tumours is well documented [5, 35, 51, 61]. We also make the following reasonable mathematical assumptions for the model:

- We assume that the tumour is perfectly spherical in shape and that it has grown in a radially symmetric manner.
- We assume that the tumour has reached its diffusion-limited avascular maximum size and consists of a large internal necrotic core surrounded by a thin layer of proliferating cells at the surface. The thin layer of live cells essentially defines the surface of the solid tumour.
- We assume that the production of the growth promoting and growth inhibitory factors is restricted to the thin layer of live, proliferating cells at the tumour surface.

Some of the assumptions of the model may be relaxed without affecting the main results of the model. For example, (i) the growth factors may be considered to be produced and/or distributed throughout the interior of the tumour. This would correspond, for example, to the case of a spheroid which had not quite reached its state of dormancy or an *in vivo* carcinoma of around 250–500 μm in diameter, where the cells in the interior of the tumour were still viable and proliferating; (ii) the tumour may be non-spherical in shape. Both of these situations would require more general 3D domains to be studied numerically and this would require modifying and extending the numerical scheme of Section 3. However, the theoretical analysis of [12] on fully 3D spherical domains indicates that the final distribution of chemicals at the surface of a sphere would be similar to those results obtained in the previous section.

The mathematical model we therefore propose consists of a system of reaction-diffusion equations on the surface of a sphere (that is, the tumour surface), modelling the interaction of the growth-promoting and growth-inhibiting chemicals which are produced by the tumour cells. We denote the concentration of the growth-promoting factor by u (for example, EGF or IGF) and the growth-inhibiting factor by v (for example, TGF-β). Although evidence exists for the interaction between the growth inhibiting factors and the growth promoting factors identified

previously, in the absence of any detailed information regarding the specific kinetic interactions, the system we consider is given by:

$$\begin{aligned} u_t &= \Delta_* u + \gamma f(u, v), \\ v_t &= d\Delta_* v + \gamma g(u, v), \end{aligned} \tag{5.1}$$

where, as before, Δ_* is the Laplace-Beltrami operator, d, γ are positive constants and the functions $f(u, v)$, $g(u, v)$ model the interactions between the two chemicals.

Using the numerical scheme developed in Section 3, and with an appropriate choice of functions f, g, we can solve such a system on the surface of a sphere. As we have already seen, given a set of parameter values which satisfy the conditions for Turing-instability, we can obtain spatially heterogeneous steady-state distributions of the two chemicals on the surface of the tumour, thereby extending the results of [12]. We now discuss the relevance of a spatially heterogeneous chemical pre-pattern to the experimentally observed cellular heterogeneity in carcinoma and multicell spheroids, and also to the invasion characteristics of carcinoma.

It is a well-known feature of solid tumours such as carcinomas that they invade the surrounding local tissue with columns of cells projecting outward from the central mass. We suggest that while a solid tumour is in its avascular, dormant state, a steady-state chemical pre-pattern, such as was illustrated in the figures in Section 4, is set up. As has already been noted, this is feasible given the difference in timescales between the tumour growth rate and the diffusion rate of the chemicals ([11, 12]). Once angiogenesis takes place and the tumour becomes vascularized, tumour cells which are located on the surface in regions of high concentrations of the growth promoting factor will be stimulated into proliferating faster and begin to invade the local tissue through increased migration. A chemical pre-pattern of this type is also consistent with the observation that tumours can directly manipulate their local environment by secretion of the growth factors. Thus this chemical pre-pattern will not only predispose the tumour cells to higher proliferation and increased mobility but will also directly affect the local surrounding tissue as well, thus facilitating invasion of the tissue by the cells [2, 36].

Under the assumption that the rate of cell out-growth is proportional to the concentration of growth promoting chemical we can simulate the early invasion of a carcinoma. In Figure 5.1 we illustrate the possible columnar out-growths of invading cancer cells from regions of the tumour surface (that is, exophytic growth) where there is a high concentration of growth promoting factor. We have assumed that cells on the surface of the tumour which are located in regions of high concentration of growth-activating chemical will have a proliferative advantage over cells in regions of high growth-inhibiting chemical. This figure is obtained by plotting in 3D the values of the function

$$\left(1 + \epsilon \sum_{n=1}^{N-1} \sum_{|m|\le n} U_n^m(\infty) Y_n^m(\mathbf{x})\right)\mathbf{x}$$

as $\mathbf{x}$ ranges over S, where $\epsilon = 0.5$ and $U_n^m(\infty)$ are the components $(u_{12}(\mathbf{x}, 40))$ of the heterogeneous steady state computed in Experiment 4 of §4 (see figure 4.8).

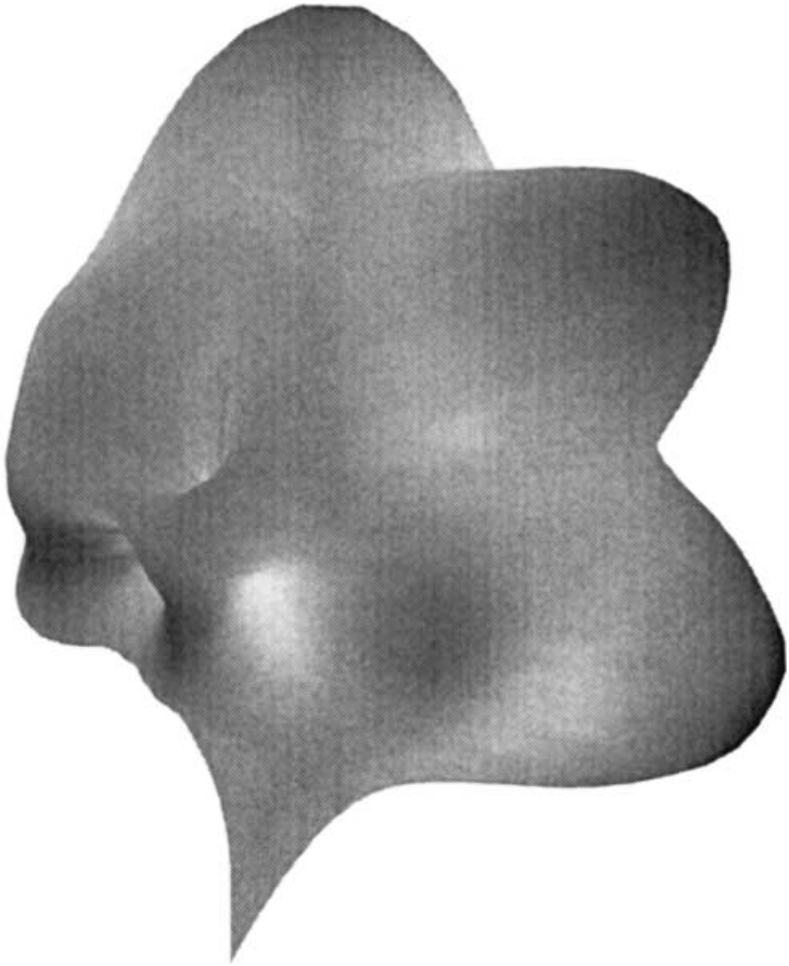

Fig. 5.1. Possible columnar outgrowths of invading cancer cells from the underlying chemical pre-pattern observed in figure 4.8 under the assumption that cells in a region of high concentration of the growth-promoting factor have a proliferative advantage.

It is clear from this figure that columns of invading cancer cells are projecting out from the central mass, as is clinically observed in carcinomas.

In the next section we further develop and extend the above model by considering a growing tumour, and posing the reaction-diffusion system on a time-dependent, growing domain.

5.2. Application to a growing spherical tumour

The results of the previous section were obtained by considering the reaction-diffusion system on a domain of fixed size, that is, the surface of the *unit sphere*. The fact that a tumour grows on a much slower timescale than the diffusion of the chemicals

enabled a genuine chemical pre-pattern to form. The model, as described, is therefore most applicable when applied to a solid tumour which has already reached its diffusion-limited avascular size. However, in the case of smaller tumours which are still growing, growth promoting and growth inhibiting chemicals will still be produced by the tumour cells. These chemicals will reach a steady-state distribution (on a faster timescale than the tumour growth rate) and a pre-pattern will be formed. If the tumour is not at the stage of its growth where invasion of the tissue occurs, then it will continue to grow, the chemicals will form a new pre-pattern (on a faster timescale) and so on. Thus a more appropriate and realistic way to model the distribution of the chemicals on the surface of a growing tumour would be to consider the reaction-diffusion system on a growing, time-dependent domain and this is what we carry out in this section.

In this case we can therefore define the surface of the tumour as a moving-boundary with radius $R(t)$, where the evolution of $R(t)$ defines the growth of the tumour. The function $R(t)$ will obey some ordinary differential equation governing the growth of the tumour (for example, the Gompertz growth law or the logistic growth law) but we are not concerned with the precise functional form here, only that $R(t)$ is some monotonically increasing function. We note that this is consistent with many previous models of avascular tumour growth (see [9] for a review). We also note that although there has been some work carried out on reaction-diffusion systems on time-dependent domains, none of these has been posed formally as a moving-boundary problem, focussing instead on uniform growth of the entire domain [4, 14, 37, 60].

We therefore now consider the application of the results of Sections 4 and 5.1 to the case of the growing domain described above. The reaction-diffusion system is therefore considered on the domain $S(t)$, the surface of the sphere of radius $R(t)$, that is, $S(t) = \{\mathbf{x} \in \mathbb{R}^3 : |\mathbf{x}| = R(t)\}$. Since, in spherical polar coordinates, (r, θ, ϕ), the Laplacian takes the form

$$\Delta = \frac{\partial^2}{\partial r^2} + \frac{2}{r}\frac{\partial}{\partial r} + \frac{1}{r^2}\Delta_*,$$

the diffusion operator on the surface of the sphere $S(t)$ is simply $\frac{1}{[R(t)]^2}\Delta_*$. The reaction-diffusion system on $S(t)$ is then

$$u_t = \frac{1}{[R(t)]^2}\Delta_* u + \gamma(a - u + u^2 v), \tag{5.2}$$

$$v_t = \frac{d}{[R(t)]^2}\Delta_* v + \gamma(b - u^2 v), \tag{5.3}$$

which is to be solved for functions u, v of θ, ϕ and t (cf. the formulation of [14]). Equivalently we can consider the system (5.2), (5.3) to be solved on $S \times [0, \infty)$, where S is the original fixed unit sphere.

It is possible to prescribe in detail the specific growth law of an avascular tumour and then couple the ODE modelling this to (5.2), (5.3). However, since we are interested only in qualitative results in this paper, it is sufficient to consider

monotonically increasing functions of time for $R(t)$, and here we restrict to the case

$$R(t) = 1 + \alpha t, \ \alpha > 0,$$

representing linear growth. The parameter α may be thought of as a nominal measure of the rate of growth, $R'(t)$, with large values of α indicating fast growth and small values of α indicating slow growth. Other forms of growth may also be considered but we consider only linear growth here.

We solved (5.2) and (5.3) using our numerical scheme in the case of linear growth, with $R(t) = 1 + 0.1t$ (the value of $\alpha = 0.1$ being chosen arbitrarily; other values of α give similar results, with the patterns appearing more slowly/quickly as α is smaller/larger). The parameter values used in the simulations were $a = 0.2, b = 1, \gamma = 5, d = 100$, chosen thus to guarantee instability. Intuitively one would expect that as the tumour grows and R increases monotonically with t, different modes will become excited. This is further substantiated when one carries out a linear stability analysis on (5.2), (5.3), the results of which show that the effect of the growing domain $R(t)$ is essentially to modify (4.5) to give

$$R^2(t)\ \gamma L(a,b,d) < k^2 < R^2(t)\ \gamma M(a,b,d)\ . \tag{5.4}$$

Thus as the domain grows, the interval of instability changes and consequently the range of wavenumbers which can become excited changes with time. Indeed from (5.4) it is expected that, for a monotonically increasing function $R(t)$, the interval of instability $[R^2(t)\gamma L,\ R^2(t)\gamma M]$ is shifted "to the right" on the k^2-axis and that higher order modes become unstable as t increases. One would therefore expect to observe a "dynamic" spatially heterogeneous pattern which evolves with time and is dominated by ever higher order modes as t increases.

Figure 5.2 shows the results of numerical simulations illustrating the specific modes which become excited with increasing time t. In this figure, using the same notation as in Section 4, we plot $U_j(t)$ against j for specific t thus indicating which particular modes have been excited (the results for $V_j(t)$ are the same). As we can see at an early time $t = 9$, essentially modes in the range $0 \leq j \leq 20$ are excited. However the dominant excited mode numbers change as time evolves and at $t = 15$ higher order modes up to $j = 45$ are becoming excited. In the last plot in the figure, at a time of $t = 21$, the amplitude of the lower modes is decreasing, there is a clear excitation of several modes in the range $70 \leq j \leq 80$ and indications that modes around $j = 110$ are becoming excited. Essentially then, as t increases, ever higher order modes are excited (as predicted above from (5.4)) indicating a dynamic pattern (slowly) evolving in time. The actual spatio-temporal distributions of the two chemicals on the surface of the tumour corresponding to the above figures are given in Figure 5.3. Clearly one can see that the spatial patterns generated are heterogeneous and change with time.

The results of these numerical simulations give a predictive insight into the "dynamic activity" which occurs during the growth of solid tumours and are consistent with the experimentally and clinically observed proliferative heterogeneity of cancer cells in solid tumours [5, 24, 35, 51, 61].

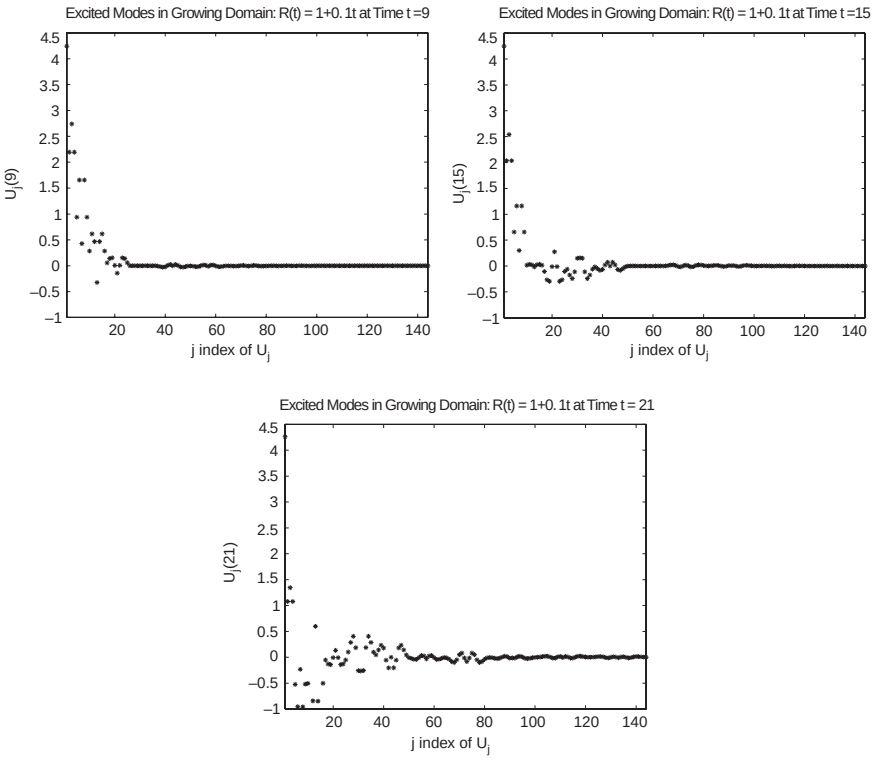

Fig. 5.2. Results of a numerical simulation in the growing tumour case. The graphs show the values of the coefficients $U_j(t)$, plotted against j, $j = 1, \ldots, 144$ for each spherical harmonic at times $t = 9$, 15 and 21. The ordering of the components $U_j(t)$ and their associated spherical harmonic Y_n^m is as per section 4. The results show that as time increases and the tumour grows higher order modes are predominantly excited.

In the computation of the growing tumour, particular care is needed to ensure that the numerical results are accurate enough to be meaningful. Since the solution is dynamically accummulating higher mode components as time increases, we may expect that numerical experiments with fixed N will become less and less accurate with increasing time. In order to check the accuracy of our numerical simulations we computed the solutions using parameters given by (4.12) above. With this choice of parameters, we may expect exponential convergence of $u_{4K}(\mathbf{x}, t)$ to $u(\mathbf{x}, t)$ (over finite time intervals) as K increases. The computed approximate errors defined in (4.13) for the growing tumour are as follows:

Table 2. Errors obtained from the accuracy test for the growing tumour calculations, calculated from (4.13).

t	$e_2(t)$	$e_3(t)$
9	2.38e-02	6.87e-04
15	8.36e-02	5.14e-03
21	3.77e-01	3.85e-02

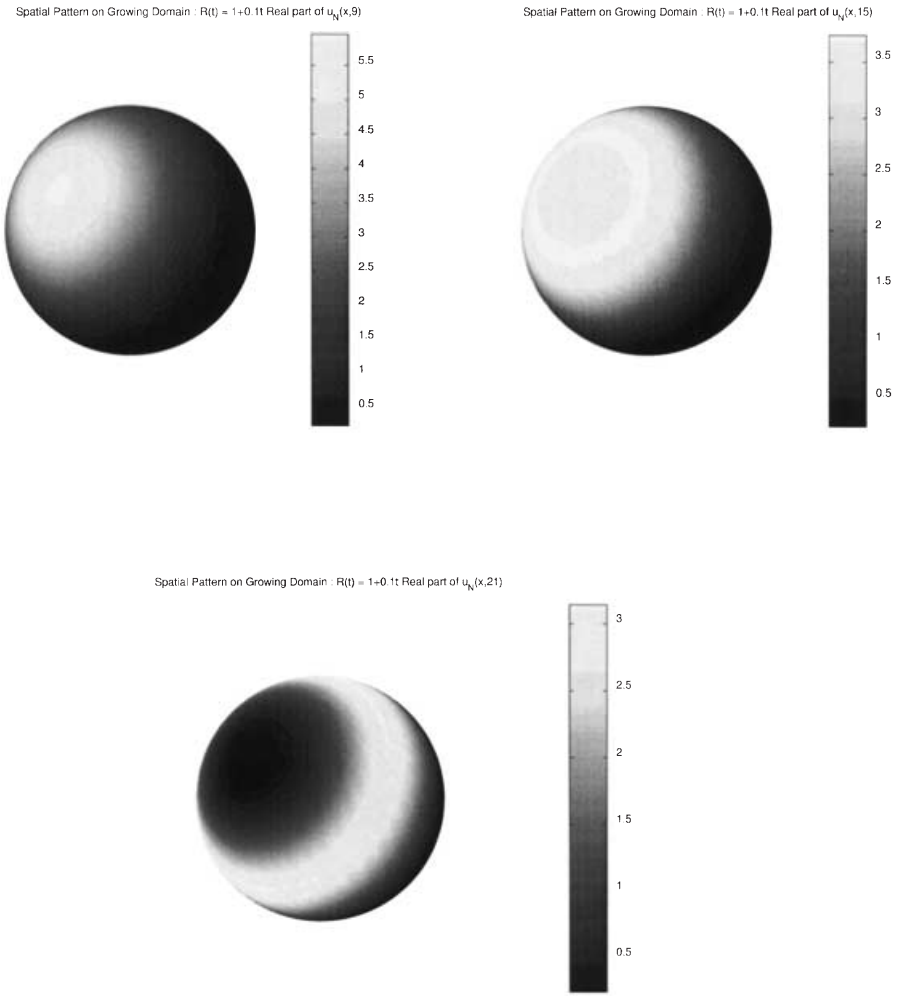

Fig. 5.3. Plots of the concentration profiles of the growth activating chemical, u, over the surface of the sphere at times $t = 9, 15$ and 21 in the situation of a growing tumour. As time increases higher order modes are excited and this is reflected in the changing chemical concentration profiles on the surface of the tumour.

These results clearly show the decreased accuracy which may be expected when we keep N and tol fixed and let t increase. They also show the increased accuracy attained by increasing K in (4.12). In particular they demonstrate that the growing tumour calculations in Figures 5.2 and 5.3 (which use $K = 3$, leading to $N = 12$) should be accurate to about 2 decimal places up to time $t = 21$. In order to maintain this level of accuracy at later times, higher values of K and N must be used which, of course, leads to an increase in computational time.

6. Discussion and conclusions

In this paper we have studied systems of reaction-diffusion equations on the surface of a sphere and have developed an appropriate numerical method for solving these systems. We have applied the pre-pattern theory (Turing-type models) of reaction-diffusion systems to a novel biological (pathological) problem – that of the growth of solid tumours, for example, carcinomas – and, moreover, have suggested a number of specific chemicals which may be involved in this process. Finally, we have studied the system of reaction-diffusion equations on a growing domain using a moving-boundary formulation. This formulation models the dynamic process of tumour growth more realistically.

The numerical method which was developed here is based on the spectral method of lines with the addition of the novel feature of a fast and efficient implementation of the reaction kinetics using Fast Fourier Transforms. This was shown to reduce the number of operations involved in the numerical calculations of the kinetics from $O(N^4)$ to $O(N^3 \log N)$ operations. From the numerical experiments performed, the method appeared robust and gave very reasonable run-times. When tested against the predictions of a linear stability analysis, the numerical results agreed well with the predicted spatially heterogeneous steady states. We note that in principle the method may be extended to other non-Euclidean domains (for example, more general manifolds and non-spherical surfaces), permitting more accurate modelling of (in our application) solid tumour growth.

We have also shown in this paper that the spatially heterogeneous chemical pre-patterns which arise on the surface of a sphere may be an important process occurring in solid tumour growth and may help to explain certain clinically and experimentally observed phenomena in carcinoma and multicell spheroids, that is, the heterogeneous distributions of proliferating cells in carcinoma and multicell spheroids and the characteristic invasive patterns of these cancers. Of course there are many other factors and processes which are involved in tumour growth, for example, the distribution of nutrient supply to the cancer cells. These are also very important and we certainly do not claim that the results of the model provide a complete answer to the problem of cancer growth and invasion but rather may be an important part of the complex overall mechanisms governing solid tumour growth (cf. [53, 54, 58, 69]).

To this end, we note that there are several features of solid tumour growth which suggest that a reaction-diffusion mechanism may be operating. First of all, there are actually present in this system identifiable chemicals which both promote and inhibit the growth of tumour cells. We have identified a number of chemicals known to be produced by tumour cells (that is, the autocrine production of growth factors) which have growth promoting and growth inhibitory effects on cell proliferation. In addition to the opposite effects on cell proliferation (promotion and inhibition), we have also shown that there is experimental evidence that certain of these chemicals interact with each other. Next, the time scale for the growth of a solid tumour is very slow in comparison to the time needed for a diffusing substance to reach steady state concentration and hence there is the opportunity for a genuine pre-pattern to form. There also appears to be a natural critical domain size in this system, that is,

the size of carcinoma in its diffusion-limited, avascular state. Whilst in this state, no invasion of the surrounding tissue can take place but, once vascularized, rapid exophytic growth (that is, growth from the *surface*) does occur. Finally, we note that many of the standard problems inherent in Turing models regarding robustness, that is, the same pattern must be repeated faithfully time and time again with the requirement that only a small number of patterns are selected in a robust and controlled manner, are not present in the case of solid tumour growth. The observed "invasion patterns" of *in vivo* carcinomas vary greatly from individual to individual. It is well known that cellular heterogeneity is not only observed within an individual tumour/multicell spheroid but varies from tumour to tumour. The results of figures 4.7, 4.8, 5.2, 5.3 are particularly appropriate in this respect. In these figures a range of modes was excited resulting in a highly heterogeneous (and, in the case of figures 5.2, 5.3, dynamic) distribution of chemical concentrations on the surface of the tumour.

The novel application of our system of reaction-diffusion equations to a growing, spherical domain has enabled us to model more realistically an actual growing solid tumour and we believe that the results of the numerical simulations of Section 5.2 are highly consistent with in vitro experimentally observed proliferative heterogeneity of cancer cells in solid tumours at all stages of their development [5, 24, 35, 51, 61]. We also believe that the results of the numerical simulations are consistent with actual in vivo clinical observations. Although we have been unable to find data such as the real-time growth profile of an actual *in vivo* tumour, it is clear from the plethora of illustrations in pathology text books, for example [25, 47], that many solid tumours grow from an initially solid central mass of tumour cells into an amorphous invading mass with many columns of cells projecting out from the surface (cf. Figure 5.1). It is not unreasonable to suggest therefore that the early and intermediate shapes and forms of these invading cancers are similar to those predicted by our model.

Finally, the results of the model suggest that some degree of control or regulation of cancer invasion may be possible through manipulation of the levels of growth factors as has already been suggested experimentally by [2, 36, 66], that is, it may be possible to intervene with the growth factor kinetics in such a way as to ensure that, even if one cannot halt the growth of a cancer, one may be able to prevent the highly heterogeneous distributions of proliferating cells from occurring [20, 21, 45, 59, 71]. Given that a solid tumour can be detected at an early enough stage in its development (for example, the avascular stage), this fact alone may prevent the irregular spread of columns of cancer cells into the surrounding tissue and may reduce the likelihood of the secondary spread of the disease.

Acknowledgements. Part of this work was carried out while the third author was a visiting fellow in the School of Mathematics, University of New South Wales under the School's Computational Mathematics Special Research Grant. The work of the first author was partly supported by a SHEFC Research Development Grant (099). The authors gratefully acknowledge this support.

Appendix: Simplified error analysis

In this appendix we give a brief error analysis for the numerical method (3.11) for (1.1). For ease of exposition we consider only the scalar case:

$$u_t = D\Delta_* u + f(u), \tag{A.1}$$

to be solved for $u : S \times [0, \infty) \to \mathbb{R}$, with $D > 0$ and $f : \mathbb{R} \to \mathbb{R}$ given, subject to

$$u(\mathbf{x}, 0) = u_0(\mathbf{x}), \quad \mathbf{x} \in S. \tag{A.2}$$

However all the results given here can be extended in an obvious way to the case of a system ($s > 1$ in (1.1)).

Although there is a large literature on spectral methods for parabolic equations on Euclidean domains (for example, [72]), these do not apply directly to the equations on the unit sphere S of interest here and the purpose of this appendix is to explore this non-standard case. We shall assume here that (A.1) has a smooth solution u valid for $t \in [0, T]$, with some finite T and we shall obtain estimates for the accuracy of our numerical method on $[0, T]$. Using different arguments (such as in [27]) it should also be possible to obtain results on the long time behaviour of our scheme.

Before we can describe the numerical analysis of (A.1), we first need to recall some elementary facts about spherical harmonic approximation on S. An excellent reference for the results discussed here is [23].

Spherical harmonics: elementary properties

Let L_2 denote the space of square-integrable complex-valued functions on S. This is a Hilbert space with inner product and norm:

$$(v, w) = \int_S v\overline{w}\,, \quad \|v\|_{L_2} = (v, v)^{1/2}\,.$$

The spherical harmonics Y_n^m , $|m| \le n$, $n \in \mathbb{N}$ defined in §2 are a complete orthonormal sequence in L_2, that is, for each $v \in L_2$,

$$v = \sum_{n=0}^{\infty} \sum_{|m|\le n} \hat{v}_n^m Y_n^m\,, \quad \text{where} \quad \hat{v}_n^m = (v, Y_n^m)\,. \tag{A.3}$$

Thus, equivalent definitions of the inner product and norm on L_2 are:

$$(v, w) = \sum_{n=0}^{\infty} \sum_{|m|\le n} \hat{v}_n^m \overline{\hat{w}_n^m}, \quad \|v\|_{L_2} = \left\{ \sum_{n=0}^{\infty} \sum_{|m|\le n} |\hat{v}_n^m|^2 \right\}^{1/2}. \tag{A.4}$$

For $r \in \mathbb{R}$, $r \ge 0$, the Sobolev space H^r on S can be defined as the space of all functions $v \in L_2$ such that

$$\sum_{n=0}^{\infty} \sum_{|m|\le n} (n + 1/2)^{2r} |\hat{v}_n^m|^2 < \infty\,, \tag{A.5}$$

with $\hat{v}_n^m$ as in (A.3). Again H^r is a Hilbert space with inner product

$$(v, w)_{H^r} = \sum_{n=0}^{\infty} \sum_{|m|\leq n} (n + 1/2)^{2r} \hat{v}_n^m \overline{\hat{w}_n^m} \tag{A.6}$$

and norm $\|v\|_{H^r} = (v, v)_{H^r}^{1/2}$. Since, by (2.3), we have $(-\Delta_* + 1/4)Y_n^m = (n + 1/2)^2 Y_n^m$, it follows that $(-\Delta_* + 1/4)$ is a well-defined positive definite bounded operator on H^2 and an alternative formula for the norm on H^r is:

$$\|v\|_{H^r} = \|(-\Delta_* + 1/4)^{r/2} v\|_{L_2} . \tag{A.7}$$

With χ_N as defined in §3, the orthogonal projection $\mathscr{P}_N : L_2 \to \chi_N$ is defined by the truncated Fourier series:

$$\mathscr{P}_N v = \sum_{n=0}^{N-1} \sum_{|m|\leq n} \hat{v}_n^m Y_n^m .$$

The fundamental properties of $\mathscr{P}_N$ are easy to describe using Fourier series arguments: If $v \in H^r$, then for $0 \leq s \leq r$, we have the *approximation property*:

$$\|v - \mathscr{P}_N v\|_{H^s} = \left\{ \sum_{n=N}^{\infty} \sum_{|m|\leq n} (n + 1/2)^{2s} |\hat{v}_n^m|^2 \right\}^{1/2} \leq \left(\frac{1}{N} \right)^{r-s} \|v\|_{H^r}. \tag{A.8}$$

Also, for any $v_N \in \chi_N$, we can write

$$v_N = \sum_{n=0}^{N-1} \sum_{|m|\leq n} \hat{\alpha}_n^m Y_n^m ,$$

with $\hat{\alpha}_n^m = (v_N, Y_n^m)$ and so, for $0 \leq s \leq r$, we have the *inverse estimate*:

$$\|v_N\|_{H^r} = \sum_{n=0}^{N-1} \sum_{|m|\leq n} (n + 1/2)^{2r} |\hat{\alpha}_n^m|^2 \leq (N + 1/2)^{r-s} \|v_N\|_{H^s}. \tag{A.9}$$

The well-known addition theorem for (complex) spherical harmonics yields the identity:

$$\sum_{|m|\leq n} |Y_n^m(\mathbf{x})|^2 = \frac{2n + 1}{4\pi}, \qquad \text{for all } \mathbf{x} \in S,\ n \geq 0.$$

Then, if $v \in H^{1+\epsilon}$, $\epsilon > 0$, we can apply the Cauchy-Schwarz inequality to the left-hand equation in (A.3) to obtain a *Sobolev embedding* result

$$|v(\mathbf{x})| \leq \left\{ \sum_{n=0}^{\infty} (n + 1/2)^{-2(1+\epsilon)} \sum_{|m|\leq n} |Y_n^m(\mathbf{x})|^2 \right\}^{1/2} \|v\|_{H^{1+\epsilon}} \leq C_\epsilon \|v\|_{H^{1+\epsilon}}, \tag{A.10}$$

where C_ϵ denotes a constant independent of v. Combining this with (A.9) it follows that for $v_N \in \chi_N$, there exists a constant C'_ϵ such that

$$\|v_N\|_\infty \leq C'_\epsilon N^{1+\epsilon} \|v_N\|_{L_2}\,, \quad N \geq 0. \tag{A.11}$$

As well as these properties of spherical harmonics, we shall also need the following rudimentary vector calculus on the manifold S. Introduce the usual spherical polar coordinates: $\mathbf{x} = (\sin\theta\cos\phi, \sin\theta\sin\phi, \cos\theta)^T$, $(\theta, \phi) \in [0, \pi]\times[0, 2\pi]$ and the spherical gradient (see [23, page 13])

$$\nabla_* v(\mathbf{x}) = \hat{\mathbf{e}}_1 \frac{1}{\sin\theta}\frac{\partial v}{\partial \phi} + \hat{\mathbf{e}}_2 \frac{\partial v}{\partial \theta},$$

where $\hat{\mathbf{e}}_1 = (-\sin\phi, \cos\phi, 0)^T$, $\hat{\mathbf{e}}_2 = (\cos\theta\cos\phi, \cos\theta\sin\phi, -\sin\theta)^T$. For these we have *Green's first identity* (see [23, page 16]):

$$-\int_S (\Delta_* v) w = \int_S \nabla_* v . \nabla_* w =: (\Delta_* v, \nabla_* w), \tag{A.12}$$

which is valid for all $v \in H^2$ and $w \in H^1$. With these preliminaries we can now analyse the method introduced in §3 for the model equation (A.1).

Spectral method for (A.1)

Returning to (A.1) (which we assume to have a smooth solution u), multiplying by a test function v, integrating over S and using (A.12), we see that $u = u(\mathbf{x}, t)$ is a solution of the weak formulation:

$$(u_t, v) = -D(\nabla_* u, \nabla_* v) + (f(u), v)\,, \quad \text{for all } v \in H^1,\ t > 0\,, \tag{A.13}$$

subject to initial condition (A.2). Our numerical method (in analogy with (3.11)) for (A.13) is to seek $u_N = u_N(\mathbf{x}, t)$ with $u_N(\cdot, t) \in \chi_N$ for all $t \geq 0$, such that

$$((u_N)_t, v_N) = -D(\nabla_* u_N, \nabla_* v_N) + (f(u_N), v_N)_M\,, \quad \text{for all } v_N \in \chi_N\,,\ t > 0, \tag{A.14}$$

subject to

$$u_N(\mathbf{x}, 0) = u_0(\mathbf{x}), \quad \mathbf{x} \in S. \tag{A.15}$$

Here $(\cdot, \cdot)_M$ is the discrete inner product as defined in (3.9). For convenience we assume here that $u_0 \in \chi_N$ so that writing (A.15) makes sense. This is the case in all our numerical experiments in this paper. The extension to arbitrary smooth initial data is straightforward [72]. Then, by writing

$$u_N(\mathbf{x}, t) = \sum_{n=0}^{N-1} \sum_{|m|\leq n} (\hat{u}_N(t))_n^m Y_n^m(\mathbf{x}), \tag{A.16}$$

(A.14) can be reduced to a nonlinear system of ODEs for the coefficients $(\hat{u}_N(t))_n^m$. If we assume that f is Lipschitz in a neighbourhood of the range of u then this system has a unique solution for large enough N (see, for example, [72]).

For the analysis of (A.14), (A.15) it is useful to introduce the function $\tilde{u}_N(\cdot, t) := \mathscr{P}_N\{u(\cdot, t)\}$, for $t > 0$. Using (A.12) it is easy to prove that for all t, $\tilde{u}_N(t)$ is also the "elliptic projection":

$$(\nabla_* \tilde{u}_N, \nabla_* v_N) = (\nabla_* u, \nabla_* v_N) \,, \quad \text{for all} \quad v_N \in \chi_N. \tag{A.17}$$

Setting $\rho_N = u - \tilde{u}_N$, we then have, on recalling (A.8) and noticing that $(\tilde{u}_N)_t = \mathscr{P}_N u_t$,

$$\|\rho_N\|_{L_2} \leq \left(\frac{1}{N}\right)^r \|u\|_{H^r}, \quad \|(\rho_N)_t\|_{L_2} \leq \left(\frac{1}{N}\right)^r \|u_t\|_{H^r}. \tag{A.18}$$

(Note that the norm on S of a function of $(\mathbf{x}, t) \in S \times [0, \infty)$ is a function of t.)

The convergence of the solution u_N of (A.14), (A.15) will depend on an appropriate choice of the integer M in the discrete inner product $(\cdot, \cdot)_M$ appearing in (A.14). For the purposes of this simplified error analysis we shall consider only the case when M can be chosen so that

$$(f(v_N), w_N) = (f(v_N), w_N)_M \quad \text{for all} \quad v_N, w_N \in \chi_N. \tag{A.19}$$

For example if f is polynomial of degree p, then $f(v_N)w_N$ has degree $(p+1)(N-1)$ and (since (3.8) has degree of precision $M-2$) the choice $M \geq 2 + (p+1)(N-1)$ will ensure that (A.19) holds.

Theorem A.1 *Suppose that f is Lipschitz in a neighbourhood of the range of u and suppose that M is chosen so that (A.19) holds. Then for $t \in [0, T]$, we have the superalgebraic error estimate for the method (A.14) applied to (A.13):*

$$\|u(\cdot, t) - u_N(\cdot, t)\|_{L_2} \leq C \left(\frac{1}{N}\right)^r \int_0^T \{\|u(\cdot, \tau)\|_{H^r} + \|u_t(\cdot, \tau)\|_{H^r}\} \, d\tau,$$

for any $r \geq 0$ where C is a constant which may depend on T and r.

Proof. We begin by writing $u - u_N = \rho_N + \theta_N$, where $\theta_N = \tilde{u}_N - u_N$. Then we have, for all $v_N \in \chi_N$,

$$\begin{aligned}((\theta_N)_t, v_N) + D(\nabla_* \theta_N, \nabla_* v_N) = {} & ((\tilde{u}_N)_t, v_N) + D(\nabla_* \tilde{u}_N, \nabla_* v_N) \\ & -((u_N)_t, v_N) - D(\nabla_* u_N, \nabla_* v_N).\end{aligned}$$

Using (A.14), (A.17) and then (A.13) we have for all $v_N \in \chi_N$,

$$\begin{aligned}((\theta_N)_t, v_N) + D(\nabla_* \theta_N, \nabla_* v_N) &= ((\tilde{u}_N)_t, v_N) + D(\nabla_* \tilde{u}_N, \nabla_* v_N) - (f(u_N), v_N)_M \\ &= ((\tilde{u}_N)_t, v_N) + D(\nabla_* u, \nabla_* v_N) - (f(u_N), v_N)_M \\ &= (f(u), v_N) - (f(u_N), v_N)_M - ((\rho_N)_t, v_N).\end{aligned}$$

Hence with $v_N = \theta_N$ and using $D > 0$, we have

$$\begin{aligned}\frac{1}{2}\frac{d}{dt}\|\theta_N\|_{L_2}^2 &\leq |(f(u), \theta_N) - (f(u_N), \theta_N)_M| + \|(\rho_N)_t\|_{L_2}\|\theta_N\|_{L_2} \\ &\leq |(f(u) - f(u_N), \theta_N)| + |(f(u_N), \theta_N) - (f(u_N), \theta_N)_M| \\ &\quad + \|(\rho_N)_t\|_{L_2}\|\theta_N\|_{L_2} \,. \end{aligned} \tag{A.20}$$

Now the arguments in [72] show that there is no loss of generality in assuming that u_N lies in the neighbourhood of u in which f is Lipschitz continuous. Using this assumption (with Lipschitz constant γ) on the first term on the right-hand side of (A.20) and the assumption that M is consistent with f in the second yields

$$\frac{1}{2}\frac{d}{dt}\|\theta_N\|_{L_2}^2 \leq \left\{\gamma\|u-u_N\|_{L_2} + C_r\left(\frac{1}{N}\right)^r \|u_N\|_{L_2} + \|(\rho_N)_t\|_{L_2}\right\}\|\theta_N\|_{L_2}. \tag{A.21}$$

Hence, for some constant C,

$$\frac{d}{dt}\|\theta_N\|_{L_2} \leq C\left\{\|\theta_N\|_{L_2} + \left(\frac{1}{N}\right)^r \|u\|_{L_2} + \|\rho_N\|_{L_2} + \|(\rho_N)_t\|_{L_2}\right\}. \tag{A.22}$$

Then, since $\theta_N(\mathbf{x}, 0) = 0$, the proof is completed by combining Grönwall's lemma with the estimates (A.18). □

Remark. It is clear from the above proof that the requirement (A.19) can be weakened by requiring instead that the inequality

$$|(f(v_N), w_N) - (f(v_N), w_N)_M| \leq C\left(\frac{1}{N}\right)^r \|v_N\|_{L_2}\|w_N\|_{L_2} \tag{A.23}$$

holds for all v_N and $w_N \in \chi_N$, with v_N in a neighbourhood of u. When f is sufficiently smooth (but not necessarily polynomial) it is still possible to derive formulae for M which ensure that (A.23) holds.

References

1. Alberts, B., Bray, D., Lewis, J., Raff, M., Roberts, K., Watson, J.D.: Molecular Biology of the Cell (3rd ed.) Garland Publishing, New York, (1994)
2. Albo, D., Berger, D.H., Wang, T.N., Xu, X.L., Rothman, V., Tuszynski, G.P.: Thrombospondin-1 and transforming-growth-factor-beta1 promote breast tumor cell invasion through up-regulation of the plasminogen/plasmin system. Surgery **122**, 493–499 (1997)
3. Anderson, A.R.A., Chaplain, M.A.J., Newman, E.L., Steele, R.J.C., Thompson, A.M.: Mathematical modelling of tumour invasion and metastasis, J. theor. Med., **2**, 129–154 (2000)
4. Arcuri, P., Murray, J.D.: Pattern sensitivity to boundary and initial conditions in reaction-diffusion models, J. Math. Biol., **24**, 141–165 (1986)
5. Becciolini, A., Balzi, M., Barbarisi, M., Faraoni, P., Biggeri, A., Potten, C.S.: 3H-thymidine labelling index (TLI) as a marker of tumour growth heterogeneity: evaluation in human solid carcinomas, Cell Prolif., **30**, 117–126 (1997)
6. Britton, N.F.: Reaction-Diffusion Equations and their Application to Biology. Academic Press, New York, (1986)
7. Byrne, H.M., Chaplain, M.A.J.: Growth of non-necrotic tumours in the presence and absence of inhibitors. Math. Biosci., **130**, 151–181 (1995)
8. Byrne, H.M., Chaplain, M.A.J.: Growth of necrotic tumours in the presence and absence of inhibitors. Math. Biosci., **135**, 187–216 (1996)
9. Byrne, H.M., Chaplain, M.A.J.: Free boundary value problems associated with the growth and development of multicellular spheroids. Euro. Jnl of Applied Mathematics **8**, 639–658 (1997)

10. Chao, C.C., Hu, S.X., Sheng, W.S., Tsang, M., Peterson, P.K.: Tumor-necrosis-factor-alpha mediates the release of bioactive transforming-growth-factor-beta in murine microglial cell-cultures. Clin. Immun. Immunopath., **77**, 358–365 (1995)
11. Chaplain, M.A.J., Benson, D.L., Maini, P.K.: Nonlinear diffusion of a growth inhibitory factor in multicell spheroids, Math. Biosci., **121**, 1–13 (1994)
12. Chaplain, M.A.J.: Reaction-diffusion prepatterning and its potential role in tumor invasion, J. Bio. Sys., **3**, 929–936 (1995)
13. Chen, T.C., Hinton, D.R., Apuzzo, M.L.J., Hofman, F.M.: Differential effects of tumor-necrosis-factor-alpha on proliferation, cell-surface antigen expression and cytokine interactions in malignant gliomas, Neurosurgery **32**, 85–94 (1993)
14. Crampin, E.J., Gaffney, E.A., Maini, P.K.: Reaction and diffusion on growing domains: Scenarios for robust pattern formation, Bull. Math. Biol., **61**, 1093–1120 (1999)
15. Cullen, K.J., Yee, D., Sly, W.S., Perdue, J., Hampton, B., Lippman, M.E., Rosen, N.: Insulin-like growth factor receptor expression and function in human breast cancer. Cancer Res., **50**, 48–53 (1990)
16. DeKepper, P., Castets, V., Dulos, E., Boissonade, J.: Turing-type chemical-patterns in the chlorite-iodide-malonic acid reaction. Physica D **49**, 161–169 (1991)
17. Danforth, D.N., Sgagias, M.K.: Tumor-necrosis-factor-alpha enhances secretion of transforming-growth-factor-beta (2) in MCF-7 breast-cancer cells, Clin. Canc. Res., **2**, 827–835 (1996)
18. Dillon, R., Maini, P.K., Othmer, H.G.: Pattern formation in generalized Turing systems. I. Steady-state patterns in systems with mixed boundary conditions. J. Math. Biol., **32**, 345–393 (1994)
19. Driscoll, J.R., Healy, D.M.: Computing Fourier transforms and convolutions on the 2-sphere, Advances in Applied Mathematics **15**, 202–250 (1994)
20. Ellis, M.J., Jenkins, S., Hanfelt, J., Redington, M.E., Taylor, M., Leek, R., Siddle, K., Harris, A.: Insulin-like growth factors in human breast cancer. Breast Cancer Res. Treat., **52**, 175–184 (1998)
21. Ethier, S.P.: Growth factor synthesis and human breast cancer progression. J. Natl. Cancer Inst., **87**, 964–973 (1995)
22. Fortunato, S.J., Menon, R., Lombardi, S.J.: Interleukin-10 and transforming-growth-factor-beta inhibit amniochorion tumor-necrosis-factor-alpha production by contrasting mechanisms of action: Therapeutic implications in prematurity, Amer. J. Obst. Gyn., **177**, 803–809 (1997)
23. Freeden, W., Gervens, T., Schreiner, M.: Constructive Approximation on the Sphere with Applications to Geomathematics, Clarendon Press, Oxford, (1998)
24. Freyer, J.P., Sutherland, R.M.: Proliferative and clonogenic heterogeneity of cells from EMT6/Ro multicellular spheroids induced by the glucose and oxygen supply, Cancer Res., **46**, 3513–3520 (1986)
25. Govan, A.D.T., MacFarlane, P.S., Callander, R.: Pathology Illustrated (4th Edition). Churchill Livingstone, Edinburgh, (1995)
26. Hata, A., Shi, Y.G., Massagué, J.: TGF-β signaling and cancer: structural and functional consequences of mutations in Smads. Molecular Medicine Today **4**, 257–262 (1998)
27. Humphries, A.R., Stuart, A.M.: Dynamical Systems and Numerical Analysis, Cambridge University Press, Cambridge, (1996)
28. Hunding, A.: Dissipative structures in reaction-diffusion systems: numerical determination of bifurcations in the sphere, J. Chem. Phys., **72**, 5241–5248 (1980)
29. Hunding, A.: Bifurcations of nonlinear reaction-diffusion systems in prolate spheroids, J. Math. Biol., **17**, 223–239 (1983)
30. Hunding, A.: Bifurcations of nonlinear reaction-diffusion systems in oblate spheroids, J. Math. Biol., **19**, 249–263 (1984)

31. Hunding, A.: Morphogen prepatterns during mitosis and cytokinesis in flattened cells: Three dimensional Turing structures of reaction-diffusion systems in cylindrical coordinates, J. theor. Biol., **114**, 571–588 (1985)
32. Hunding, A.: Pattern formation of reaction-diffusion systems in 3-space coordinates – Supercomputer simulation of drosophila morphogenesis. Physica A **188**, 172–177 (1992)
33. Ito, R., Kitadai, Y., Kyo, E., Yokozaki, H., Yasui, W., Yamashita, U., Nikai, H., Tahara, E.: Interleukin 1α acts as an autocrine growth stimulator for human gastric carcinoma cells. Cancer Res., **53**, 4102–4106, (1993)
34. Iversen, O.H.: The hunt for endogenous growth-inhibitory and or tumor suppression factors – their role in physiological and pathological growth-regulation. Adv. Cancer Res., **57**, 413–453 (1991)
35. Jannink, I., Risberg, B., Vandiest, P.J., Baak, J.P.A.: Heterogeneity of mitotic-activity in breast-cancer, Histopathol., **29**, 421–428 (1996)
36. Keski-Oja, J., Postlethwaite, A.E., Moses, H.L.: Transforming growth factors and the regulation of malignant cell growth and invasion. Cancer Invest., **6**, 705–724 (1988)
37. Kulesa, P.M., Cruywagen, G.C., Lubkin, S.R., Maini, P.K., Sneyd, J., Ferguson, M.W.J., Murray, J.D.: On a model mechanism for the spatial patterning of teeth primordia in alligator, J. theor. Biol., **180**, 287–296 (1996)
38. Malik, S.T.A., Griffin, D.B., Fiers, W., Balkwill, F.R.: Paradoxical effects of tumour necrosis factor in experimental ovarian cancer, Int. J. Cancer **44**, 918–925 (1989)
39. Massagué, J.: TGFβ signal transduction. Annu. Rev. Biochem., **67**, 753–791 (1998)
40. Meinhardt, H.: Models of Biological Pattern Formation. Academic Press, London, (1982)
41. Meinhardt, H.: The Algorithmic Beauty of Sea Shells. (2nd enlarged edition; with PC-software) Springer, Heidelberg, New York, (1998)
42. Mohlenkamp, M.J.: A Fast Transform for Spherical Harmonics, Ph.D. Dissertation, Yale University, (1997)
43. Mooney, J.R.: Simulation of a reaction-diffusion system on large dimpled surfaces using a vector computer. Math. Comput. Simul., **28**, 209–225 (1986)
44. Moses, M.L., Yang, E.Y., Pietenpol, J.A.: TGF-β stimulation and inhibition of cell proliferation: new mechanistic insights. Cell **63**, 245–247 (1990)
45. Mueller, M.M., Herold-Mende, C.C., Riede, D., Lange, M., Steiner, H.-H., Fusenig, N.E.: Autocrine growth regulation by granulocyte colony-stimulating factor and granulocyte macrophage colony-stimulating factor in human gliomas with tumor progression, Am. J. Pathol., **155**, 1557–1567 (1999)
46. Mueller-Klieser, W.: Multicellular spheroids: A review on cellular aggregates in cancer research, J. Cancer Res. Clin. Oncol., **113**, 101–122 (1987)
47. Muir, R., MacSween (ed.), R.N.M., Whaley (ed.), K.: Muir's Textbook of Pathology (13th edition), Edward Arnold, London, (1992)
48. Murray, J.D.: Parameter space for Turing instability in reaction diffusion mechanisms: a comparison of models, J. theor. Biol., **98**, 143–163 (1982)
49. Murray, J.D.: Mathematical Biology (Second Edition) Springer-Verlag, London, (1993)
50. Nagy, N., Vanky, F.: Transforming-growth-factor-beta, (TGF beta), secreted by the immunogenic ex vivo human carcinoma cells, counteracts the activation and inhibits the function of autologous cytotoxic lymphocytes. Pretreatment with interferon gamma and tumor-necrosis-factor-alpha reduces the production of active TGF beta. Canc. Immunol. Immunother., **45**, 306–312 (1998)
51. Palmqvist, R., Oberg, A., Bergstrom, C., Rutegard, J.N., Zackrisson, B., Stenling, R.: Systematic heterogeneity and prognostic significance of cell proliferation in colorectal cancer, Br. J. Cancer **77**, 917–925 (1998)

52. Pang, X.P., Yoshimura, M., Wang, J.Y., Dubinett, S.M.: TNF-alpha induced antiproliferation is not dependent on the autocrine action of TGF-beta-1 in a thyroid-cancer, Lymphokine Cytokine Res., **13**, 93–97 (1994)
53. Pusztai, L., Lewis, C.E., Yap (eds.), E.: Cell Proliferation in Cancer: Regulatory Mechanisms of Neoplastic Cell Growth, Oxford University Press, Oxford, (1996)
54. Quinn, K.A., Treston, A.M., Unsworth, E.J., Miller, M.-J., Vos, M., Grimley, C., Battey, J., Mulshine, J.L., Cuttitta, F.: Insulin-like growth factor expression in human cancer cell lines, J. Biol. Chem., **271**, 11477–11483 (1996)
55. Rahimi, N., Tremblay, E., McAdam, L., Roberts, A., Elliott, B.: Autocrine secretion of TGF-beta 1 and TGF-beta 2 by pre-adipocytes and adipocytes: A potent negative regulator of adipocyte differentiation and proliferation of mammary carcinoma cells, In Vitro Cell. Dev. Biol. Animal **34**, 412–420 (1998)
56. Romieu, R., Lacabanne, V., Kayibanda, M., Antoine,B., Bennoun,M., Chouaib, S., Guillet, J.G., Viguier, M.: Critical stages of tumor growth regulation in transgenic mice harboring a hepatocellular carcinoma revealed by distinct patterns of tumor-necrosis-factor-alpha and transforming-growth-factor-beta mRNA production, Internat. Immun., **9**, 1405–1413 (1997)
57. Rose, D.M., Winston, B.W., Chan, E.D., Riches, D.W.H., Henson, P.M.: Interferon-gamma and transforming-growth-factor-beta modulate the activation of mitogen-activated protein kinases and tumor-necrosis-factor-alpha production induced by Fc gamma-receptor stimulation in murine macrophages, Biochem. Biophys. Res. Commun., **238**, 256–260 (1997)
58. Rosfjord, E.C., Dickson, R.B.: Growth factors, apoptosis and survival of mammary epithelial cells. J. Mammary Gland Biol. Neoplasia **4**, 229–237 (1999)
59. Rozengurt, E.: Autocrine loops, signal transduction and cell cycle abnormalities in the molecular biology of lung cancer. Curr. Opin. Oncol., **11**, 116–122 (1999)
60. Saunders, P.T., Ho, H.W.: Reliable segmentation by successive bifurcation, Bull. Math. Biol.,**57**, 539–556 (1995)
61. Sessa, F., Bonato, M., Bisoni, D., Bosi, F., Capella, C.: Evidence of a wide heterogeneity in cancer cell population in gallbladder adenocarcinomas, Lab. Invest., **76**, 860 (1997)
62. Shampine, L.F., Reichelt, M.W.: The MATLAB ODE Suite, SIAM J. Sci. Comput., **18**, 1–22 (1997)
63. Simonitsch, I., Krupitza, G.: Autocrine self-elimination of cultured ovarian cancer cells by tumor necrosis factor alpha (TNF-alpha), Br. J. Cancer **78**, 862–870 (1998)
64. Snoeck, H.W., Weekx, S., Vanbockstaele, D.R., Lardon, F., Nys, G., Lenjou, M., Berneman, Z.N.: Tumor-necrosis-factor-alpha is a potent synergistic stimulator of very primitive adult human CD34++CD38– bone-marrow cells, and antagonizes the inhibitory effects of transforming-growth-factor-beta, but not of interferon-gamma, Blood **86**, (S1) 31 (1995)
65. Stroud, A.H.: Approximate Calculation of Multiple Integrals Prentice Hall, Englewood Cliffs, (1973)
66. Suganuma, M., Okabe, S., Sueoka, E., Iida, N., Komori, A., Kim, S.J., Fujiki, H.: New process of cancer prevention mediated through inhibition of tumor-necrosis-factor-alpha expression, Cancer Res., **56**, 3711–3715 (1996)
67. Sutherland, R.M.: Cell and environment interactions in tumor microregions: the multicell spheroid model, Science **240**, 177–184 (1988)
68. Szabo, G., Mandrekar, P., Girouard, L., Catalano, D.: Regulation of human monocyte functions by acute ethanol treatment – decreased tumor-necrosis-factor-alpha, interleukin-1-beta and elevated interleukin-10, and transforming-growth-factor-beta production, Alcohol. Clin. Exp. Res., **20**, 900–907 (1996)

69. Tahara, E., Yasui, W., Yokozaki, H.: Abnormal growth factor networks in neoplasia, chapter 6, pp. 133–153, in: L. Pusztai, C.E. Lewis and E. Yap (eds.). Cell Proliferation in Cancer: Regulatory Mechanisms of Neoplastic Cell Growth, Oxford University Press, Oxford, (1996)
70. Takahashi, J.A., Mori, H., Fukumoto, M., Igarashi, K., Jaye, M. Oda, Y., Kikuchi, H., Hatanaka, M.: Gene expression of fibroblast growth factors in human gliomas and meningiomas: demonstration of cellular source of basic fibroblast growth factor mRNA and peptide in tumor tissues. Proc. Natl. Acad. Sci. USA, **87**, 5710–5714 (1990)
71. Thiery, J.P., Chopin, D.: Epithelial cell plasticity in development and tumor progression. Cancer Metastasis Rev., **18**, 31–42 (1999)
72. Thomée, V.: Galerkin Finite Element Methods for Parabolic Problems, Springer-Verlag, New York, (1997)
73. Tricoli, J.V., Rall, L.B., Karakousis, C.P., Herrera, L., Petrelli, N.J., Bell, G.I., Shows, T.B., Enhanced levels of insulin-like growth factor messenger RNA in human colon carcinomas and liposarcomas. Cancer Res., **46**, 6169–6173 (1986)
74. Turing, A.M.: The chemical basis of morphogenesis, Phil. Trans. Roy. Soc. Lond., **B237**, 37–72 (1952)
75. Vrana, J.A., Strang, M.T., Grande, J.P., Getz, M.J.: Expression of tissue factor in tumor stroma correlates with progression to invasive human breast-cancer – paracrine regulation by carcinoma cell-derived members of the transforming-growth-factor-beta family, Cancer Res., **56**, 5063–5070 (1996)
76. Westermark, B., Heldin, C.-H.: Platelet-derived growth factor in autocrine transformation. Cancer Res., **51**, 5087–5092 (1991)
77. Wibe, E., Lindmo, T., Kaalhus, O.: Cell kinetic characteristics in different parts of multicellular spheroids of human origin, Cell Tissue Kinet., **14**, 639–651 (1981)
78. Wu, S., Boyer, C.M., Whitaker, R.S., Berchuck, A., Wiener, J.R., Wienberg, J.B., Bast, R.C.: Tumor-necrosis-factor-alpha as an autocrine and paracrine growth-factor for ovarian cancer – monokine induction of tumor-cell proliferation and tumor-necrosis-factor-alpha expression. Cancer Res., **53**, 1939–1944 (1993)
79. Yanagihara, K., Tsumuraya, M.: Transforming growth factor $\beta 1$ induces apoptotic cell death in cultured human gastric carcinoma cells. Cancer Res., **52**, 4042–4045 (1992)
80. Yoshida, K., Kyo, E., Tsujino, T., Sano, T., Niimoto M., Tahara, E.: Expression of epidermal growth factor, transforming growth factor-α and their receptor genes in human carcinomas: implication for autocrine growth. Cancer Res., **81**, 43–51 (1990)
81. Zeki, K., Nakano, Y., Inokuchi, N., Watanabe, K., Morimoto, I., Yamashita, U., Eto, S.: Autocrine stimulation of interleukin 1 in the growth of a human thyroid carcinoma cell line, NKM 1. J. Clin. Endocrinol. Metab., **176**, 127–133 (1993)